



# CoNi based alloy/oxides@N-doped carbon core-shell dendrites as complementary water splitting electrocatalysts with significantly enhanced catalytic efficiency



Qing Zhang<sup>a</sup>, Xiao Lin Li<sup>a</sup>, Bai Xiang Tao<sup>a</sup>, Xiao Hu Wang<sup>a</sup>, Yang Hui Deng<sup>a</sup>, Xiao Ying Gu<sup>a</sup>, Ling Jie Li<sup>b</sup>, Wei Xiao<sup>c</sup>, Nian Bing Li<sup>a,\*</sup>, Hong Qun Luo<sup>a,\*</sup>

<sup>a</sup> School of Chemistry and Chemical Engineering, Southwest University, Chongqing 400715, PR China

<sup>b</sup> School of Chemistry and Chemical Engineering, Chongqing University, Chongqing 400044, PR China

<sup>c</sup> Cengong County Agriculture Bureau, Cengong, Guizhou 557800, PR China

## ARTICLE INFO

### Keywords:

Co<sub>0.75</sub>Ni<sub>0.25</sub> alloy  
Hierarchical dendrite  
Core-shell architecture  
N-doped carbon  
Water splitting

## ABSTRACT

Highly active, earth-abundant, and stable electrocatalysts are indispensable for overall water splitting. In this work, hierarchical dendrite-like Co<sub>0.75</sub>Ni<sub>0.25</sub> alloy prepared by a simple hydrothermal reduction route can serve as a high-performance catalyst for hydrogen evolution reaction. The synergistic effect from Co and Ni atoms optimizes the catalytic behavior of their alloy, and the hierarchical dendrite structure enlarges the contact area with the electrolyte, exposing more active sites. Based on the dendrite-like Co<sub>0.75</sub>Ni<sub>0.25</sub> alloy, we further fabricate a core-shell architecture with the conductive N-doped carbon shell coated dendrite-like CoNi/CoNiO<sub>2</sub> nanocomposites via a calcination process at 600 °C (CoNi/CoNiO<sub>2</sub>@NC-600). The dendrite-like CoNi/CoNiO<sub>2</sub>@NC-600 displays significantly improved activity of oxygen evolution reaction due to large active surface area, high conductivity, and the continuous electron transfer among metal, metal oxide, and N-doped carbon. Furthermore, the dendrite-like Co<sub>0.75</sub>Ni<sub>0.25</sub> alloy and CoNi/CoNiO<sub>2</sub>@NC-600 are assembled into a water splitting electrolyzer with a low voltage of 1.51 V to drive a current density of 10 mA cm<sup>-2</sup>.

## 1. Introduction

Electrochemical water splitting into hydrogen and oxygen as an attractive way for sustainable energy conversion and storage has been widely applied [1,2]. Effective water splitting needs to expedite the sluggish kinetics processes by high-active and strong-stable catalysts which can substantially lower the activation energy barrier of both oxygen evolution reaction (OER) and hydrogen evolution reaction (HER) [3]. As commercial electrocatalysts, noble metal (Pt) and noble metal oxides (RuO<sub>2</sub>) possess unique superiorities in catalysis toward HER and OER, respectively, while the cost and rareness greatly limited their large-scale and practical applications in water splitting [4,5]. With further research breakthroughs, a large number of non-noble metal materials (e.g., transition metal hydroxides [6,7], oxides [8,9], chalcogenides [10,11], carbides [12,13], and phosphides [14,15], as well as their alloys [16,17]) have been regarded as efficient HER and OER electrocatalysts with high performance, high abundance, and low cost. Among these, alloys exhibit superior HER electrocatalytic activity and durability compared to single metal materials. A series of M-M1 (M, M1

= Co, Fe, Cu, Ni, and Mo) binary alloys were widely studied and it was found that Co-Ni alloys possess attractive HER performance among these alloys due to the synergistic interactions of Co and Ni [18,19]. However, it is still a challenge to develop CoNi-based alloys with a particular morphology and further improve their catalytic activities and utilization efficiency. The catalytic activity of materials is greatly affected by the morphology, structure, and the number of active sites. Thus, it is necessary to pay close attention to design some electrocatalysts with unique morphology and to effectively regulate the size and shape of structure. Previous considerable efforts have been devoted to the fabrication of different morphologies, such as cube, nanoparticle, nanosheet, and nanowire of CoNi-based nanostructures that showed high electrocatalytic activity [20–23]. Nevertheless, the fabrication of hierarchical dendrite-like CoNi alloy was rarely reported. Those catalysts with fractal structures can not only provide large available surface area, but also facilitate the mass transport and gas diffusion [24]. Lin, et al. synthesized shape-controlled hierarchical Pt dendrites that display better HER performance than commercial Pt/C [25].

In addition, to realize efficient overall water splitting, overcoming

\* Corresponding authors.

E-mail addresses: [linb@swu.edu.cn](mailto:linb@swu.edu.cn) (N.B. Li), [luohq@swu.edu.cn](mailto:luohq@swu.edu.cn) (H.Q. Luo).

the kinetic sluggish of electrocatalyst from OER is also a crucial research issue. Earth-abundant transition metal oxides, like Co and Ni-based oxides (e.g., CoO [26], NiO [27], Co<sub>3</sub>O<sub>4</sub> [28], Ni<sub>x</sub>Fe<sub>3-x</sub>O<sub>4</sub> [29], etc.), are considered as efficient catalysts for OER due to the inherent corrosion resistance in alkali aqueous electrolyte and the multiple valence states [30]. For example, FeCo oxide nanosheets with a large specific surface area required an overpotential of 308 mV to achieve 10 mA cm<sup>-2</sup> [31]. However, the low conductivity and wide-band-gap of pure transition metal oxides significantly hampered the transport of electrons or protons during the oxidation process [29]. To improve the OER catalytic performance of these materials, integrating metal with metal oxides could be a feasible strategy to further improve the electrical conductivity of catalytic centers. A number of excellent studies have proven that the interactions between metal and metal oxides are highly beneficial to the catalytic activity of OER [29]. For example, Ni/NiO and Co/Co<sub>3</sub>O<sub>4</sub> core/shell hybrids needed overpotentials of 90 and 145 mV at the current density of 10 mA cm<sup>-2</sup>, respectively [32,33].

Herein, we synthesized a series of CoNi alloys with different Co/Ni ratios via a facile hydrothermal reduction method. It was found that the Co<sub>0.75</sub>Ni<sub>0.25</sub> alloy with hierarchical dendrite structure showed high activity for HER. This special hierarchical structure can expose more active sites, enlarge the contact area with electrolytes, and facilitate the binding and transport of proton. Based on the dendrite structure, the Co<sub>0.75</sub>Ni<sub>0.25</sub> alloy dendrite was further carbonized at 600 °C to obtain a core-shell architecture with the N-doped carbon shell coated CoNi/CoNiO<sub>2</sub> dendrite (CoNi/CoNiO<sub>2</sub>@NC-600) that showed significantly improved activity and stability for OER. The complementary water-splitting electrolyzer constructed with dendrite-like Co<sub>0.75</sub>Ni<sub>0.25</sub> alloy and CoNi/CoNiO<sub>2</sub>@NC-600 shows excellent catalytic performance.

## 2. Experimental

### 2.1. Synthesis of the Co<sub>0.75</sub>Ni<sub>0.25</sub> alloy dendrites

The Co<sub>0.75</sub>Ni<sub>0.25</sub> alloy dendrites were synthesized by a hydrothermal reduction method. 0.75 mmol of CoCl<sub>2</sub>·6H<sub>2</sub>O, 0.25 mmol of NiCl<sub>2</sub>·6H<sub>2</sub>O, 4 mmol (0.2 M) of sodium citrate, and 10 mmol of NaOH were dissolved in 20 mL of deionized water and stirred about 10 min until a purple solution was obtained. Next, 2.5 mL of N<sub>2</sub>H<sub>4</sub>·H<sub>2</sub>O (85%) was added to the purple solution and the mixture was transferred into a 50 mL Teflon-lined stainless steel autoclave and kept at 160 °C (120 and 200 °C) for 2 h. After the autoclave naturally cooled to ambient temperature, the black precipitate was collected with the magnet, washed with ultrapure water and ethanol for several times, and then dried at 60 °C to obtain Co<sub>0.75</sub>Ni<sub>0.25</sub> alloy dendrites.

For comparison, the metallic Co, Co<sub>0.5</sub>Ni<sub>0.5</sub> alloy, Co<sub>0.25</sub>Ni<sub>0.75</sub> alloy, and metallic Ni samples were synthesized by a similar procedure as mentioned above through changing the molar ratio of NiCl<sub>2</sub>·6H<sub>2</sub>O and CoCl<sub>2</sub>·6H<sub>2</sub>O (n NiCl<sub>2</sub>·6H<sub>2</sub>O + m CoCl<sub>2</sub>·6H<sub>2</sub>O = 1 mmol).

### 2.2. Synthesis of the CoNi/CoNiO<sub>2</sub>@NC dendrites

A portion of 40 mg of CoNi alloy dendrites and 20 mg of dopamine hydrochloride were dispersed into 10 mL of Tris-buffer solution (pH = 8.5) with continuous stirring for 3 h. Then, the precipitate was collected with the magnet, washed with ultrapure water and ethanol for two times, respectively, and dried at 60 °C overnight. The precursor products were then annealed at 600 °C for 1 h in N<sub>2</sub> gas with a heating rate of 5 °C min<sup>-1</sup> to be transformed to CoNi/CoNiO<sub>2</sub>@NC-600 dendrites. In addition, the precursor products were also annealed at various temperatures (300, 400, 500, and 700 °C).

### 2.3. Electrochemical measurements

All electrochemical tests were performed on a workstation (CHI 660E) with a standard three-electrode system in 1.0 M KOH solution,

using carbon cloth (CC) with the catalysts as the working electrode, a graphite rod as a counter electrode, and Ag/AgCl electrode as the reference electrode. The catalyst ink was prepared by dissolving 5 mg of catalyst in 300 μL of ethanol containing 40 μL of Nafion and was then slowly loaded onto carbon cloth (1 cm<sup>2</sup>) and dried at room temperature. The mass loading for each sample was approximately 2.0 mg cm<sup>-2</sup> on a carbon cloth. The current density was calibrated corresponding to the geometric area of working electrode (1 cm<sup>2</sup>). Linear sweep voltammetry (LSV) was conducted with a scan rate of 5 mV s<sup>-1</sup>. Electrochemical impedance spectroscopy (EIS) was carried out in the frequency range of 10<sup>-2</sup> to 10<sup>5</sup> Hz with an amplitude of 5 mV. The long-time durability was tested at a fixed potential by chronoamperometric measurement. The recorded potentials in our work were normalized from the equation: E (RHE) = E (Ag/AgCl) + (0.2012 + 0.059 pH) V. The Tafel slopes were derived from a linear fit utilizing the Tafel equation ( $\eta = b \log j + a$ , where  $\eta$  is the overpotential,  $b$  is the Tafel slope, and  $j$  is the current density).

### 2.4. ECSA measurement

The ECSA values were calculated by the electrochemical double-layer capacitance (C<sub>dl</sub>). To measure C<sub>dl</sub> value, cyclic voltammetry (CV) curves were performed in the non-Faradaic regions at scan rates of 20, 40, 60, 80, and 100 mV s<sup>-1</sup>. Then, the ECSA was calculated by ECSA = C<sub>dl</sub>/C<sub>s</sub>, where C<sub>s</sub> is the specific capacitance using an average value of 0.040 m F cm<sup>-2</sup> referred to literature reports [34].

### 2.5. Turnover frequency calculation

To calculate the turnover frequency (TOF, s<sup>-1</sup>), we used the following formula [35]:

$$\text{TOF} = (j \times A) / (2 \times F \times n) \quad (1)$$

where number 2 means 2 electrons were required to form 1 mol H<sub>2</sub> molecule, A (cm<sup>2</sup>) is the geometric area of a carbon cloth electrode, j (A cm<sup>-2</sup>) is the current density obtained by LSV measurements at overpotential of 200 and 300 mV, n is moles amount of coated metal atom, and F is the Faraday constant (96,485.3 C mol<sup>-1</sup>).

### 2.6. Faraday efficiency determination

The gas generated from water splitting in an H-type electrolytic cell was quantitatively determined using gas chromatography (GC, Agilent-7890, USA) with the external standard method. The ultrapure Ar gas was delivered into the whole system before running the experiment. The average evolution rates of H<sub>2</sub> and O<sub>2</sub> can be acquired according to the generated gas amount in unit electrolysis time. The Faraday efficiency (FE) was acquired according to the following formula [36]:

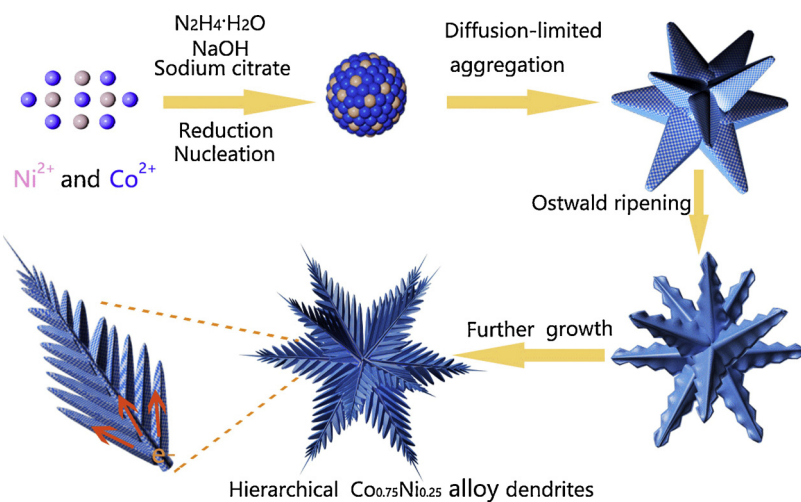
$$\text{FE} = z \times n \times F / (I \times t) \times 100\% \quad (2)$$

where z is the electron transfer number, n is the amount (moles) of the generated gas in the experiment, F is the Faraday constant (96485.3 C mol<sup>-1</sup>), I is the applied constant current (A), and t is the electrolysis time (s).

## 3. Results and discussion

### 3.1. Structure characterizations and HER performance of Co<sub>0.25</sub>Ni<sub>0.75</sub> alloy dendrites

The formation mechanism of the Co<sub>0.75</sub>Ni<sub>0.25</sub> alloy dendrites is depicted in Scheme 1. First, with the help of sodium citrate, Co<sup>2+</sup> and Ni<sup>2+</sup> ions were slowly released to reduce into primary CoNi alloy nuclei during a hydrothermal process (Fig. S1a). Under the influence of diffusion-limited aggregation [37], the nanoparticles in these nuclei



**Scheme 1.** Schematic illustration of the formation mechanism of hierarchical  $\text{Co}_{0.75}\text{Ni}_{0.25}$  alloy dendrites.

gradually grew along the same crystallographic orientation to form disperse bud-shape structures extending from nucleus center (Fig. S1b), which is a non-equilibrium and diffusion controlled kinetic process that is favorable for the fractal growth [37]. Then, these bud-shape structures began to grow hierarchically a lot of branches through the coarsening (Fig. S1c), also known as Ostwald ripening [25,38]. Finally, more perfect dendrite structures with acuminate edges can be obtained. All the CoNi alloy samples can be easily collected by magnetic separation due to the strong magnetism (Fig. S2). The  $\text{Co}_x\text{Ni}_{1-x}$  alloy samples with different molar ratios of Co/Ni including 4:0, 3:1, 2:2, 1:3, and 0:4 were synthesized, and their ratios were also quantified by the energy dispersive X-ray spectroscopy (EDS, see Fig. S3) and inductively coupled plasma optical emission spectrometry (ICP-OES, see Table S1).

As-prepared alloys with different molar ratios of Co/Ni present apparent morphology difference by scanning electron microscopy (SEM) images (Fig. 1). The pure metallic Co shows overall dendrite structure with an average length about 15  $\mu\text{m}$  (Fig. 1a), and the individual dendrite (inset of Fig. 1a) has a main branch that further develops dozens of smaller leaves on both sides. These irregularly accumulative dendrites are easy to develop into oversize superstructures. On the contrary, pure metallic Ni doesn't show dendrite morphology, but a

bunch of intertwined fibers (Fig. 1b). The magnified image shows that the fibers are composed of cross-linked nanoparticles (inset of Fig. 1b). When the molar ratio of Co/Ni is controlled at 3:1, obtained  $\text{Co}_{0.75}\text{Ni}_{0.25}$  alloy not only maintains regular dendrite structure, but also forms 3D flower-like dendrites with divergent branches growing from the nucleus center (Fig. 1c, 1d). Their main branches shorten to about 3  $\mu\text{m}$  of length, which is several times smaller than that of main branches of pure metallic Co. In addition, the small branches on both sides of the main branch grow more symmetrically and tightly, looking like a piece of hierarchical palm leaf (inset of Fig. 1d). With the increase of Ni content,  $\text{Co}_{0.5}\text{Ni}_{0.5}$  and  $\text{Co}_{0.25}\text{Ni}_{0.75}$  alloy show the irregular morphology characteristics combining both particle-shape and bud-shape structures (Fig. 1e, f). From the above, Co species tends to grow into dendrite superstructure, while Ni species tends to form nanofiber structure. An appropriate molar ratio of Co/Ni (3:1) can obtain the regular, small-size, and divergent  $\text{Co}_{0.75}\text{Ni}_{0.25}$  alloy dendrites by controlling the competitive effect of the crystallization for Co atom and Ni atom. The effect of hydrothermal temperature on the morphology of  $\text{Co}_{0.75}\text{Ni}_{0.25}$  alloy was explored at a lower temperature of 120 °C and a higher temperatures of 200 °C. However, compared with  $\text{Co}_{0.75}\text{Ni}_{0.25}$  alloys prepared at 160 °C, they show the inferior uniformity and

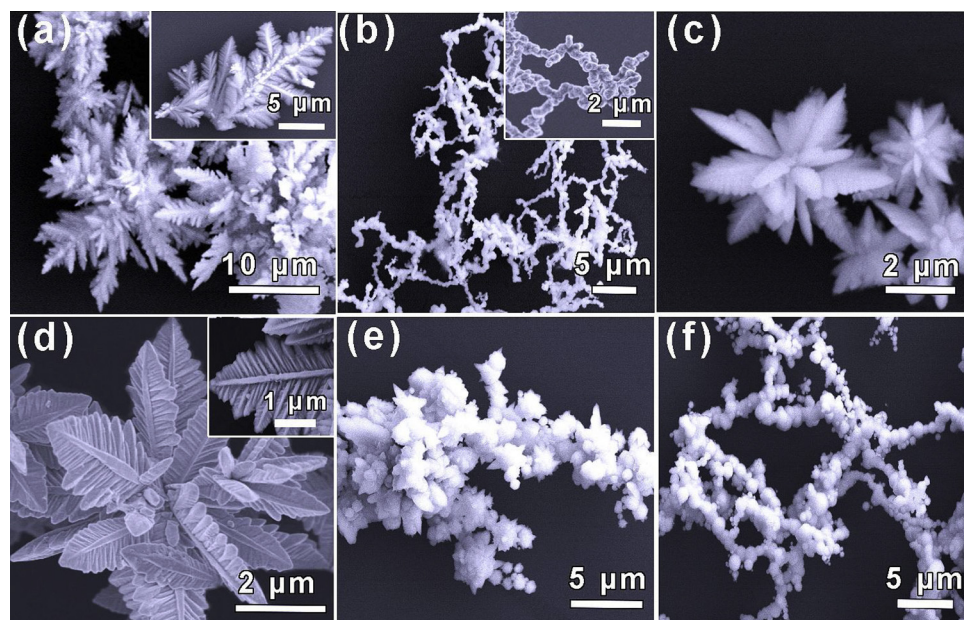


**Fig. 1.** (a) SEM image and magnified SEM image (inset) of the pure metallic Co. (b) SEM image and magnified SEM image (inset) of the pure metallic Ni. (c) Side-view SEM image and (d) top-view SEM image of  $\text{Co}_{0.75}\text{Ni}_{0.25}$  alloy dendrites, the inset of (d) displays the magnified SEM image of single  $\text{Co}_{0.75}\text{Ni}_{0.25}$  alloy dendrite. (e) SEM image of  $\text{Co}_{0.5}\text{Ni}_{0.5}$  alloy. (f) SEM image of  $\text{Co}_{0.25}\text{Ni}_{0.75}$  alloy.

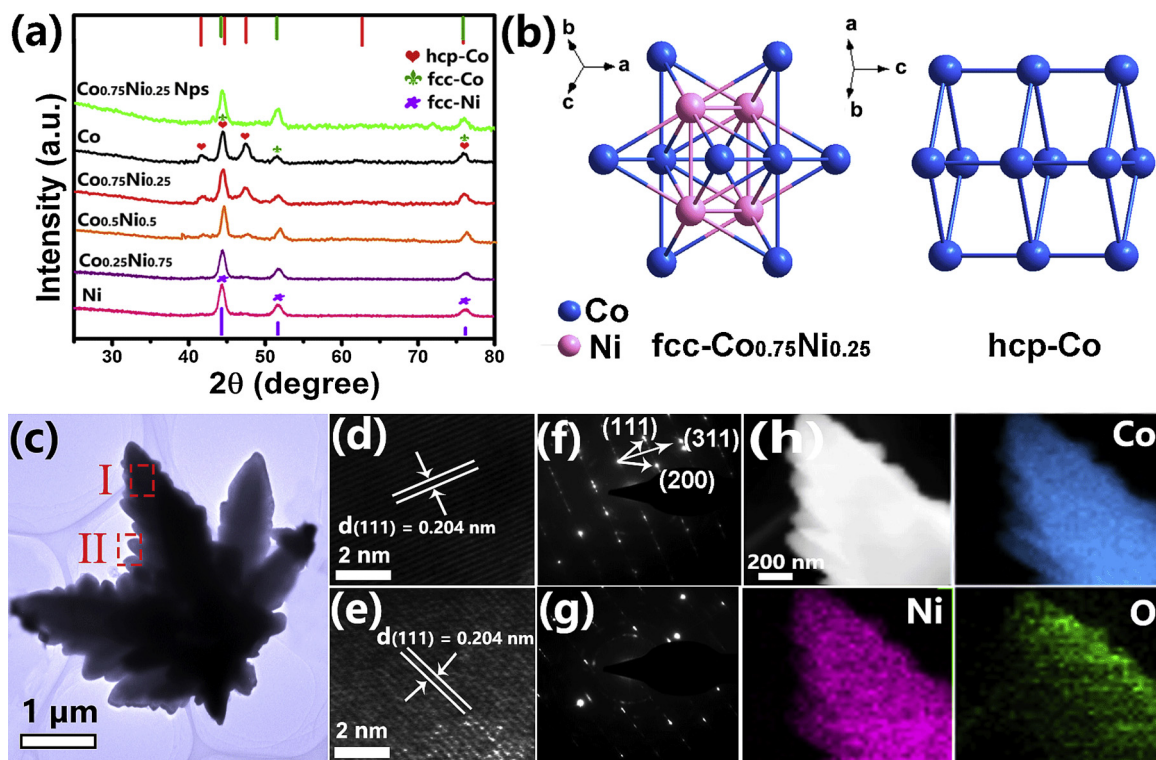


**Fig. 2.** (a) XRD patterns of the pure metallic Co, pure metallic Ni, Co<sub>0.25</sub>Ni<sub>0.75</sub> alloy, Co<sub>0.5</sub>Ni<sub>0.5</sub> alloy, Co<sub>0.75</sub>Ni<sub>0.25</sub> alloy, and Co<sub>0.75</sub>Ni<sub>0.25</sub> alloy nanoplates (labeled as Co<sub>0.75</sub>Ni<sub>0.25</sub> Nps). (b) The crystal structure of a single unit cell of fcc Co<sub>0.75</sub>Ni<sub>0.25</sub> and hcp Co (111) surface. (c) TEM image of Co<sub>0.75</sub>Ni<sub>0.25</sub> alloy dendrites. HRTEM image of Co<sub>0.75</sub>Ni<sub>0.25</sub> alloy dendrites for the boxed area I (d) and II (e) in (c). The corresponding SAED pattern of Co<sub>0.75</sub>Ni<sub>0.25</sub> alloy dendrites for the boxed area I (f) and II (g) in (c). (h) DF-TEM image of Co<sub>0.75</sub>Ni<sub>0.25</sub> alloy dendrites and element mapping images of Co, Ni, and O, respectively.

completeness in dendrite structure (Fig. S4). Thus, controlling the hydrothermal temperature at 160 °C is a suitable condition for the growth of the ideal dendrite structure. Moreover, the influence of sodium citrate on the morphology was also investigated. When sodium citrate was not added during the hydrothermal process, Co<sub>0.75</sub>Ni<sub>0.25</sub> alloy displays the hexagonal-shape and polygonal-shape nanoplates (Fig. S5a, S5b). With the increased concentration of sodium citrate (0.05 and 0.1 M), just the bud-shape structures growing from nucleus center is found (Fig. S5c, S5d), but there are no hierarchical structures, revealing that sodium citrate as a structure directing and capping agent plays a crucial role for nucleation and crystal growth. Actually, in excess citrate solution, Co<sup>2+</sup> and Ni<sup>2+</sup> ions can coordinate with citrate ions to form complexes, which decreases the concentration of free Co<sup>2+</sup> and Ni<sup>2+</sup> ions in the solution and slower the kinetics of nucleation and growth of alloy [37]. Thus, the morphology and structure of the product were efficiently controlled.

Powder X-ray diffraction (XRD) analysis further reveals the crystalline information of the pure Co, the pure Ni, and other Co<sub>x</sub>Ni<sub>1-x</sub> alloy samples (Fig. 2a). The pure metallic Ni shows three diffraction peaks at 44.5°, 51.7°, 76.3° corresponding to the (111), (200), and (220) planes of the face-centered-cubic (fcc) crystal phases of Ni (JCPDS No. 04-0850). Ni-rich Co<sub>0.25</sub>Ni<sub>0.75</sub> alloy shows basically consistent peaks with the pure metallic Ni. Interestingly, the pure metallic Co reveals a mixture of the fcc and hexagonal-close-packed (hcp) crystal phases. The peaks at 41.7°, 44.5°, 47.6°, and 75.9° are related to the (100), (002), (101), and (110) planes of hcp Co (JCPDS No. 05-0727), while the three peaks at 44.5°, 51.6°, and 75.9° can be indexed to the (111), (200), and (220) planes of fcc Co (JCPDS No. 15-0806). Co-rich Co<sub>0.75</sub>Ni<sub>0.25</sub> alloy has similar peaks with the pure metallic Co, demonstrating the coexistence of fcc and hcp phases [39,40]. However, Co<sub>0.75</sub>Ni<sub>0.25</sub> alloy nanoplates (Co<sub>0.75</sub>Ni<sub>0.25</sub> Nps) without sodium citrate only mainly show the fcc phase of CoNi alloy, further indicating that sodium citrate may selectively control the surface energy of different crystal faces and favor the

formation of dendritic structure with hcp phases [41]. The crystal structures of fcc Co<sub>0.75</sub>Ni<sub>0.25</sub> and hcp Co are shown in Fig. 2b. The transmission electron microscopy (TEM) image reveals a complete dendrite structure of Co<sub>0.75</sub>Ni<sub>0.25</sub> alloy (Fig. 2c), which is in agreement with the SEM image (Fig. 1c, 1d). The high-resolution TEM (HRTEM) images of both the boxed area I and II in Fig. 2c show the lattice structures at the stem and the branch of a dendrite, and they all reveal the orderly lattice fringes with a spacing distance of 0.204 nm (Fig. 2d, 2e), corresponding to the (111) plane of the Co-Ni alloy. Moreover, the corresponding selected area electron diffraction (SAED) patterns (Fig. 2f, 2g) illustrate the single-crystalline nature of the entire Co<sub>0.75</sub>Ni<sub>0.25</sub> alloy dendrite. The dark-field TEM (DF-TEM) image and the corresponding energy dispersive X-ray (EDX) elemental mapping analysis (Fig. 2h) suggest the Ni and Co elements are uniformly distributed throughout the entire dendrite. The observed small quantity of O element mainly was derived from air and surface oxides at the boundary. The chemical composition and valence states of the Co<sub>0.75</sub>Ni<sub>0.25</sub> alloy dendrites were determined by X-ray photoelectron spectroscopy (XPS) measurement. The XPS survey spectrum of Co<sub>0.75</sub>Ni<sub>0.25</sub> alloy dendrites is displayed in Fig. 3a, and a series of peaks related to Co, Ni, and O elements can be observed. For the high-resolution Co 2p spectrum (Fig. 3b), two peaks at 778.7 eV (2p<sub>3/2</sub>) and 793.8 eV (2p<sub>1/2</sub>) can be indexed to metallic Co<sup>0</sup> [42]. The other two peaks at 780.1 eV (2p<sub>3/2</sub>) and 795.4 eV (2p<sub>1/2</sub>) can be attributed to Co<sup>2+</sup> caused by air oxidation. Likewise, two peaks at 852.3 eV (Ni 2p<sub>3/2</sub>) and 870.1 eV (Ni 2p<sub>1/2</sub>) can be indexed to metallic Ni<sup>0</sup>, while the other two peaks can also be attributed to Ni<sup>2+</sup> caused by air oxidation (Fig. 3c) [16]. In the O 1s spectrum (Fig. 3d), the peaks at 532.2 and 531.0 eV are attributed to the adsorbed molecular water and hydroxyl groups at the surface, respectively [43]. The weak peak at 529.1 eV further indicates the presence of a small amount of oxide species on the surface of the sample [16]. Apparently, based on the above XPS analysis, the oxidation of partial surface metal atoms is inevitable,

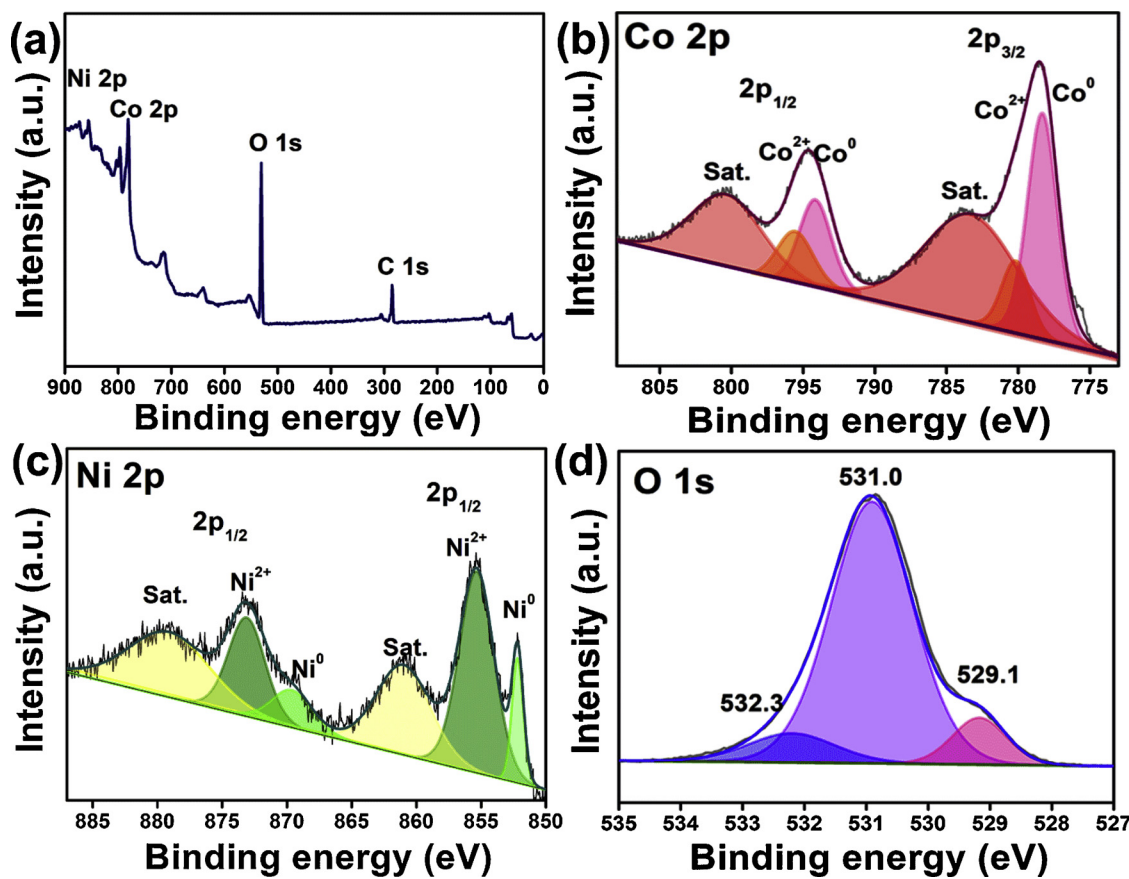


Fig. 3. (a) XPS survey of  $\text{Co}_{0.75}\text{Ni}_{0.25}$  alloy dendrites. (b-d) high resolution XPS spectra of Co 2p, Ni 2p, and O 1s.

suggesting the existence of a thin Co-Ni oxide layer on the surface of the  $\text{Co}_{0.75}\text{Ni}_{0.25}$  alloy.

The HER performance of a series of  $\text{Co}_x\text{Ni}_{1-x}$  alloy samples was evaluated in 1.0 M KOH solution by standard three-electrode systems. All samples were dropped on CC as the working electrode (labeled as  $\text{Co}_x\text{Ni}_{1-x}/\text{CC}$ ). The Pt/C (20 wt%) was also loaded onto CC to test for comparison (Pt/C/CC). From the  $iR$ -corrected polarization curves (Fig. 4a), both the pure Co/CC and pure Ni/CC show obviously lower activity than bimetallic catalysts including  $\text{Co}_{0.5}\text{Ni}_{0.5}/\text{CC}$ ,  $\text{Co}_{0.25}\text{Ni}_{0.75}/\text{CC}$ , and  $\text{Co}_{0.75}\text{Ni}_{0.25}/\text{CC}$ , suggesting the synergistic effect between Co and Ni atoms of CoNi alloys. Among  $\text{Co}_x\text{Ni}_{1-x}$  alloy samples, dendrite-like  $\text{Co}_{0.75}\text{Ni}_{0.25}/\text{CC}$  exhibits the highest catalytic activity with the overpotentials of 108 and 237 mV at the current densities of 10 and 100  $\text{mA cm}^{-2}$ , respectively, which is only inferior to the commercial Pt/C/CC and superior or at least comparable to many previously reported Co-based and Ni-based electrocatalysts for HER (Table S2). This illustrates that a proper molar ratio of metal Co and Ni in  $\text{Co}_{0.75}\text{Ni}_{0.25}$  alloy plays a crucial role in improving electrocatalytic activity toward HER. In addition, partial oxidized  $\text{Co}_{0.75}\text{Ni}_{0.25}$  alloy surface suggested by XPS analysis has a certain influence on the activity of the whole catalyst. According to previous theoretical calculations, Co and Ni metals have a proper binding energy for H atom (close to Pt) [44], and Co oxides can be hydroxylated to promote water dissociation [45]. Under the strong electrostatic affinity, OH<sup>-</sup> produced by  $\text{H}_2\text{O}$  decomposition would preferentially attach to Co-Ni oxide surface containing positively charged  $\text{Co}^{2+}$  species, then the nearby metal CoNi site would facilitate H adsorption, promoting electrochemical hydrogen adsorption process (Volmer step). Thus, the main active center in  $\text{Co}_{0.75}\text{Ni}_{0.25}$  alloy dendrite is derived from metal Co and Ni, but the inevitable thin Co-Ni oxide layer also contributes to the whole HER catalysis process to a certain extent. The HER reaction kinetics on these catalysts were further assessed by the corresponding Tafel plots (Fig. 4b). The Tafel

slope of 100 mV dec<sup>-1</sup> for  $\text{Co}_{0.75}\text{Ni}_{0.25}/\text{CC}$  suggests that the HER process on  $\text{Co}_{0.75}\text{Ni}_{0.25}/\text{CC}$  occurs through a Volmer-Heyrovsky mechanism, which is lower than that of  $\text{Co}_{0.25}\text{Ni}_{0.75}/\text{CC}$  (125 mV dec<sup>-1</sup>),  $\text{Co}_{0.5}\text{Ni}_{0.5}/\text{CC}$  (159 mV dec<sup>-1</sup>), Ni/CC (149 mV dec<sup>-1</sup>), and Co/CC (198 mV dec<sup>-1</sup>), confirming that  $\text{Co}_{0.75}\text{Ni}_{0.25}/\text{CC}$  possesses the faster kinetics of mass and electron transfer. Moreover, compared to the nanoplate-shape  $\text{Co}_{0.25}\text{Ni}_{0.75}$  alloy without sodium citrate and bud-shape  $\text{Co}_{0.25}\text{Ni}_{0.75}$  with low-concentration sodium citrate (0.05 M and 0.10 M) during the synthesis, dendrite-like  $\text{Co}_{0.75}\text{Ni}_{0.25}$  alloy with higher concentration of sodium citrate (0.2 M) still displays more excellent activity (Fig. S6), indicating that the perfect hierarchical dendrite structure can provide larger surface area and expose more active sites. The higher BET surface area of dendrite-like  $\text{Co}_{0.75}\text{Ni}_{0.25}$  ( $57 \text{ m}^2 \text{ g}^{-1}$ ) than that of nanoplate-shape  $\text{Co}_{0.25}\text{Ni}_{0.75}$  alloy ( $22 \text{ m}^2 \text{ g}^{-1}$ ) also confirms this assumption (Fig. S7). We further determined the electrochemically active surface area (ECSA) by cyclic voltammetry (CV) method (Fig. S8, Table S3). As expected, the ECSA of  $\text{Co}_{0.75}\text{Ni}_{0.25}/\text{CC}$  ( $297.5 \text{ cm}^2$ ) is significantly enhanced (Table S3), which is larger than that of  $\text{Co}_{0.5}\text{Ni}_{0.5}/\text{CC}$  ( $177.5 \text{ cm}^2$ ),  $\text{Co}_{0.25}\text{Ni}_{0.75}/\text{CC}$  ( $90.0 \text{ cm}^2$ ), Ni/CC ( $87.5 \text{ cm}^2$ ), and Co/CC ( $45.0 \text{ cm}^2$ ). The ECSA-normalized polarization curves were obtained to further understand the intrinsic activity of each active site (Fig. S9), it can be clearly seen that the  $j_{\text{ECSA}}$  of  $\text{Co}_{0.5}\text{Ni}_{0.5}/\text{CC}$  is still apparently larger than those of other  $\text{Co}_x\text{Ni}_{1-x}$  alloy samples. These evidences suggest that the enhanced surface area is a significant contribution for high HER catalytic activity, in addition, the intimate electronic interaction between different metals also plays an important role in the synergistic catalytic effects.

The turnover frequency (TOF) value can reflect closely the activity of each catalytic site of the catalysts [46]. Considering that all metal atoms are active in the catalysis, the calculated TOF values are shown in Fig. 4c and Table S4. It can be seen that  $\text{Co}_{0.75}\text{Ni}_{0.25}/\text{CC}$  exhibits the higher TOF values with  $9.42 \times 10^{-2}$  and  $8.27 \times 10^{-3} \text{ s}^{-1}$  at both 300

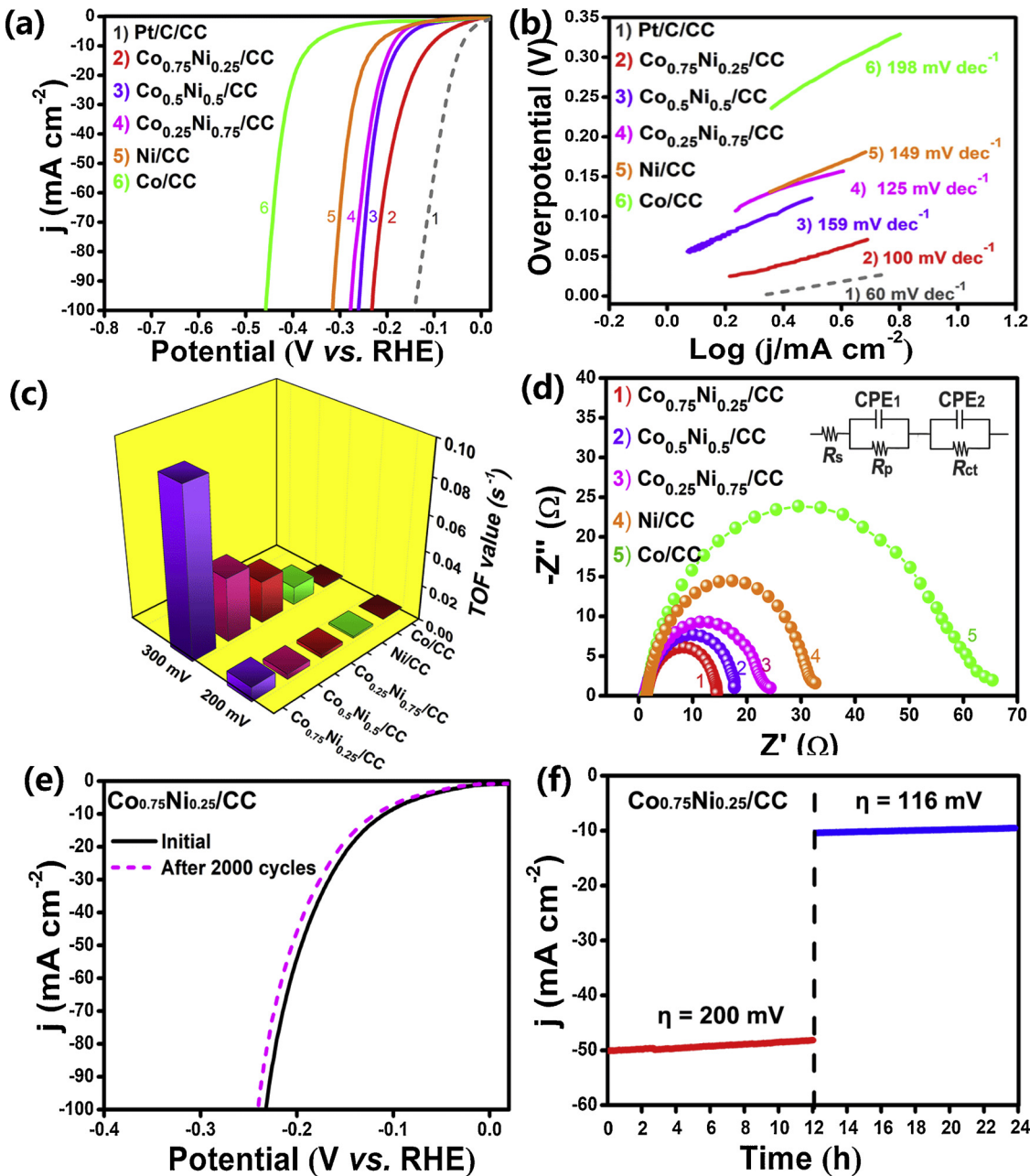


**Fig. 4.** Polarization curves (a) and Tafel plots (b) of Pt/CC, Co/CC, Ni/CC,  $\text{Co}_{0.75}\text{Ni}_{0.25}/\text{CC}$ ,  $\text{Co}_{0.5}\text{Ni}_{0.5}/\text{CC}$ , and  $\text{Co}_{0.25}\text{Ni}_{0.75}/\text{CC}$  in 1.0 M KOH. (c) Comparison of the TOF values of Co/CC, Ni/CC,  $\text{Co}_{0.75}\text{Ni}_{0.25}/\text{CC}$ ,  $\text{Co}_{0.5}\text{Ni}_{0.5}/\text{CC}$ , and  $\text{Co}_{0.25}\text{Ni}_{0.75}/\text{CC}$  for HER at 200 and 300 mV vs. RHE. (d) EIS of Co/CC, Ni/CC,  $\text{Co}_{0.75}\text{Ni}_{0.25}/\text{CC}$ ,  $\text{Co}_{0.5}\text{Ni}_{0.5}/\text{CC}$ , and  $\text{Co}_{0.25}\text{Ni}_{0.75}/\text{CC}$  at 220 mV vs. RHE, inset is the corresponding equivalent circuit model. (e) Polarization curves for  $\text{Co}_{0.75}\text{Ni}_{0.25}/\text{CC}$  before and after 2000 cycles of CV scanning. (f) Time-dependent current density curve of  $\text{Co}_{0.75}\text{Ni}_{0.25}/\text{CC}$  under the fixed overpotentials of 116 and 200 mV for 12 h, respectively.

and 200 mV than those of  $\text{Co}_{0.25}\text{Ni}_{0.75}/\text{CC}$ ,  $\text{Co}_{0.5}\text{Ni}_{0.5}/\text{CC}$ , Ni/CC, and Co/CC, respectively, indicating that more inner active sites of  $\text{Co}_{0.75}\text{Ni}_{0.25}/\text{CC}$  can be efficiently utilized. Electrochemical impedance spectroscopy (EIS) measurements were conducted at a constant overpotential of 220 mV to probe the charge transfer kinetics of interface reactions (Fig. 4d). The semicircle of the Nyquist plot attributes to the charge-transfer resistance  $R_{ct}$ . The lower  $R_{ct}$  value implies a faster reaction rate. As expected, the smallest  $R_{ct}$  (the diameter of the semicircle) of  $\text{Co}_{0.75}\text{Ni}_{0.25}/\text{CC}$  further reveals the favorable transfer kinetics and high electrical conductivity during HER processes. The durability test shows that the polarization curve of  $\text{Co}_{0.75}\text{Ni}_{0.25}/\text{CC}$  has no obvious shifting after 2000 cycles of CV scanning (Fig. 4e). In contrast, the HER activity of Ni/CC and Co/CC apparently decays with the higher increases of overpotentials of 44 and 28 mV at  $10 \text{ mA cm}^{-2}$ , respectively

(Fig. S10). The mass activity of  $\text{Co}_{0.75}\text{Ni}_{0.25}/\text{CC}$  is also better retained (85% of initial value) than Ni/CC (49%) and Co/CC (72%) from Fig. S10. The long-term electrochemical stability of  $\text{Co}_{0.75}\text{Ni}_{0.25}/\text{CC}$  was measured at the constant overpotentials of 200 and 116 mV over 12 h, respectively, the current densities only slightly decline from 50 to  $47 \text{ mA cm}^{-2}$  and from 10 to  $9.2 \text{ mA cm}^{-2}$  (Fig. 4f), further verifying a high operational durability. The XRD pattern (Fig. S11) and SEM image (Fig. S12) after stability test also reveal that  $\text{Co}_{0.75}\text{Ni}_{0.25}$  alloy composition and dendritic structure are maintained, suggesting the superior structural stability of dendrite-like  $\text{Co}_{0.75}\text{Ni}_{0.25}$  alloy. The corresponding XPS spectra of  $\text{Co}_{0.75}\text{Ni}_{0.25}$  sample after stability test (Fig. S13) further determined the contents and valences of Co and Ni on the surface. Compared to the results of fresh  $\text{Co}_{0.75}\text{Ni}_{0.25}$  alloy (Fig. 3), the Co 2p and Ni 2p spectra after stability test show a slight weakening of

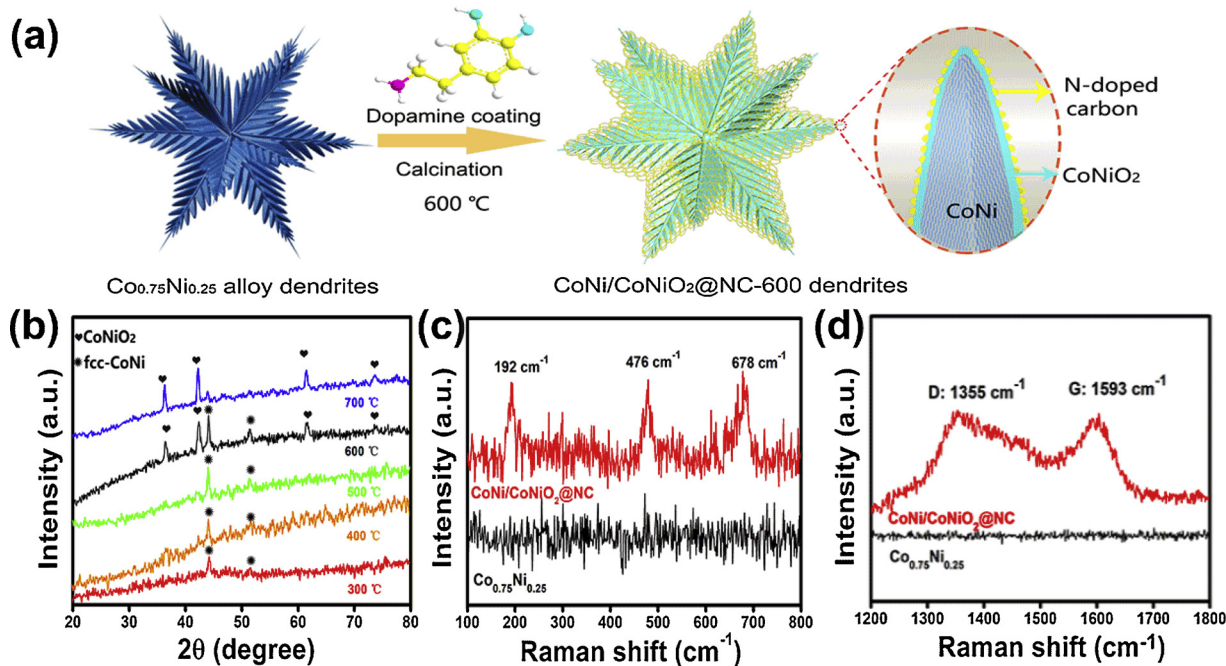


**Fig. 5.** (a) Fabrication process of the CoNi/CoNiO<sub>2</sub>@NC-600 dendrites from the Co<sub>0.75</sub>Ni<sub>0.25</sub> alloy dendrites. (b) XRD patterns of polydopamine-coated CoNi alloy dendrites annealed at 300, 400, 500, 600, and 700 °C. (c) Raman spectra of Co<sub>0.75</sub>Ni<sub>0.25</sub> alloy dendrites and CoNi/CoNiO<sub>2</sub>@NC-600 dendrites in the range of 100–800 cm<sup>-1</sup>. (d) Raman spectra of Co<sub>0.75</sub>Ni<sub>0.25</sub> alloy dendrites and CoNi/CoNiO<sub>2</sub>@NC-600 dendrites in the range of 1200–1800 cm<sup>-1</sup>.

characteristic peaks corresponding to Co<sup>0</sup> and Ni<sup>0</sup>. Table S5 lists the surface Co, Ni, and O contents of Co<sub>0.75</sub>Ni<sub>0.25</sub> alloy before and after HER stability test. The decreased Ni and Co contents after the HER stability test reveal the small loss of Co and Ni species due to the metal leaching into solution during the long-term operation, while the reduced Co/Ni ratio from 3.10 to 2.49 indicates a disproportionate loss for Co and Ni species. Co species has a higher loss than Ni species (Table S6). In addition, by comparing to the ratios of Co<sup>0</sup>/Co<sup>2+</sup> and Ni<sup>0</sup>/Ni<sup>2+</sup> before HER stability test, it is found that both the ratios of Co<sup>0</sup>/Co<sup>2</sup> and Ni<sup>0</sup>/Ni<sup>2+</sup> have a slight decrease after the stability test, which indicates that a small amount of metallic Co<sup>0</sup> and Ni<sup>0</sup> may form the surface oxide/hydroxide in alkaline environment.

### 3.2. Structure characterizations and improved OER catalytic performance of CoNi/CoNiO<sub>2</sub>@NC-600 dendrites

An efficient, abundant, and cheap non-noble metal OER electrocatalyst is equally important for a promising electrochemical water splitting device. Considering the strong corrosion resistance and stability of metal oxides in alkali solution during the OER process and the high conductivity of metals, as well as based on the unique dendrite structure of Co<sub>0.75</sub>Ni<sub>0.25</sub> alloy, the OER performance might be effectively improved by integrating metal and metal oxides. Furthermore, encapsulating transition metals into N-doped carbon material has been demonstrated to be a promising strategy for improving the OER catalytic performance [47]. The carbon shell can effectively avoid the corrosion of transition metals in acidic and alkaline solution and simultaneously accelerate the catalytic reaction on the carbon surface due to electron penetration from inner transition metals [19]. Moreover, conductive and stable N-doped carbon shell might offer a continuous highway for electron transfer throughout the entire catalyst. For instance, Co-CoO<sub>x</sub>/N-doped carbon nanocomposites display outstanding catalytic activities toward both HER and OER [41].

Based on the above analysis, we subsequently treated Co<sub>0.75</sub>Ni<sub>0.25</sub> alloy dendrites with dopamine solution to obtain polydopamine-coated CoNi alloy dendrites, and then calcined the sample at 600 °C under N<sub>2</sub> atmosphere. During the heat treatment, outer CoNi alloy was

preferentially oxidized to CoNiO<sub>2</sub>, the polydopamine coating was converted to N-doped carbon shell to coat the CoNi/CoNiO<sub>2</sub> dendrites. Finally, CoNi/CoNiO<sub>2</sub>@NC-600 dendrites were obtained (Fig. 5a). To find the optimized annealing conditions, the temperatures of the calcination process were adjusted from 300 to 400, 500, 600, and 700 °C under N<sub>2</sub> atmosphere, respectively. It is observed that the XRD patterns (Fig. 5b) of the annealed samples at 300, 400, and 500 °C show three main diffraction peaks at 44.3° and 51.5° indexed to the (111) and (200) planes of fcc CoNi alloy phase (JCPDS No. 15-0806, JCPDS No. 04-0850), demonstrating that the metallic CoNi alloy existed with fcc crystal phase. The disappearance of diffraction peaks corresponding to hcp Co phase indicates that the fcc CoNi alloy phase is more stable at high temperature [48]. When the temperature was increased to 600 °C, three new diffraction peaks at 36.8°, 42.6°, and 61.7° appeared, which can correspond to (111), (200), and (220) planes of fcc CoNiO<sub>2</sub> phase (JCPDS No. 10-0188), suggesting coexistence of CoNi alloy phase and CoNiO<sub>2</sub> phase. Further heating up to a temperature of 700 °C, only the diffraction peaks of CoNiO<sub>2</sub> are found, whereas the diffraction peaks of CoNi alloy basically disappear, indicating that CoNi alloy has been fully oxidized to CoNiO<sub>2</sub> at 700 °C. From this, it can be found that the elevated temperature is favorable for the formation of metal oxides [49], and 600 °C is a critical temperature point for achieving the coexistence of metal and metal oxides. As a contrast, polydopamine-coated CoNi alloy dendrites were also directly annealed at 600 °C in the air. The corresponding XRD pattern (Fig. S14) shows the diffraction peaks matched well with the fcc Co<sub>2</sub>NiO<sub>4</sub> phase (JCPDS No. 02-1074). Therefore, controlling the oxygen content in calcination conditions is also important for obtaining coexistence of CoNi alloy and CoNiO<sub>2</sub> instead of single Co<sub>2</sub>NiO<sub>4</sub>. Notably, the diffraction peak of carbon is difficult to be recorded because the amorphous carbon shell is thin and the peaks of the metal and metal oxide are relatively strong. The Raman spectra (Fig. 5c,d) of Co<sub>0.75</sub>Ni<sub>0.25</sub> alloy dendrites and CoNi/CoNiO<sub>2</sub>@NC-600 dendrites were carried out. As shown in Fig. 5c, Co<sub>0.75</sub>Ni<sub>0.25</sub> alloy has no any characteristic peak, implying no bond of metals with non-metals. However, for CoNi/CoNiO<sub>2</sub>@NC-600, three strong characteristic peaks located at 192, 476, and 678 cm<sup>-1</sup> can be attributed to the F<sub>2g</sub>, E<sub>g</sub>, and A<sub>1g</sub> vibrational modes, respectively, suggesting the

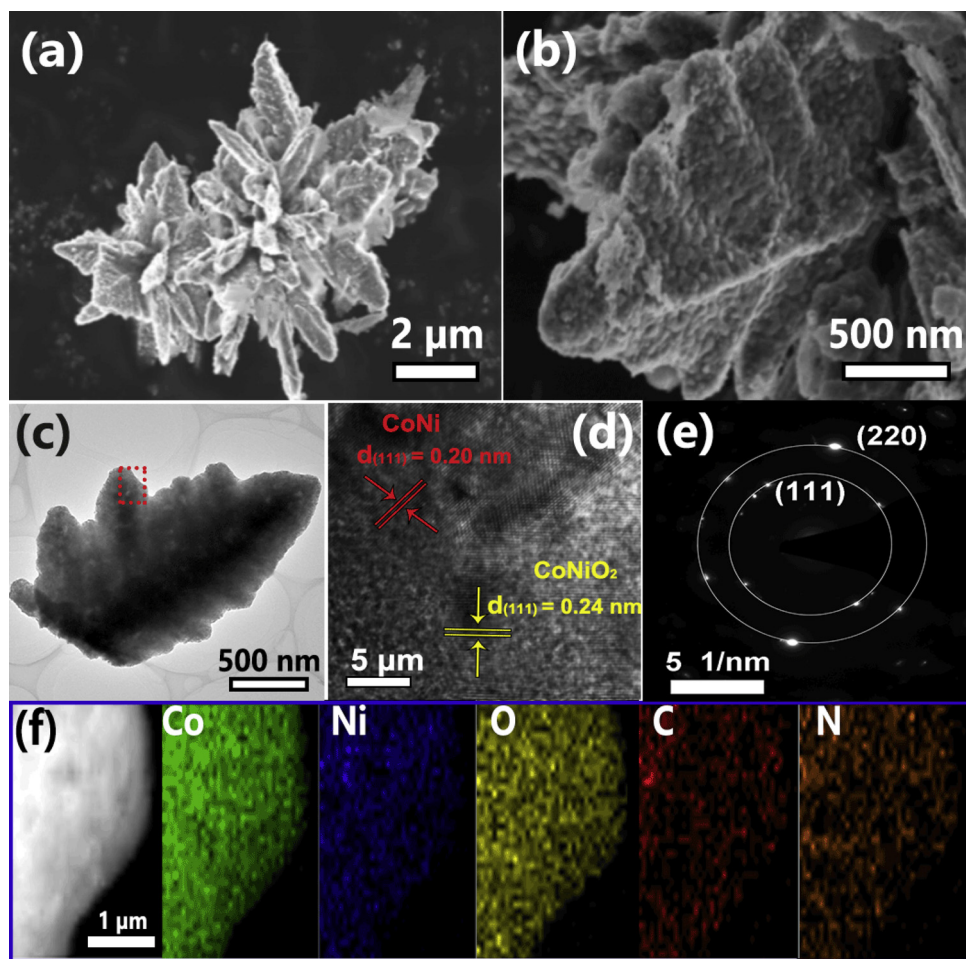


**Fig. 6.** SEM image (a) and magnified SEM image (b) of CoNi/CoNiO<sub>2</sub>@NC-600 dendrites. (c) TEM image of single CoNi/CoNiO<sub>2</sub>@NC-600 dendrite. (d) HRTEM image of CoNi/CoNiO<sub>2</sub>@NC-600 dendrite for the red boxed area in (c). (e) The corresponding SAED pattern of CoNi/CoNiO<sub>2</sub>@NC-600 dendrite. (f) DF-TEM image of CoNi/CoNiO<sub>2</sub>@NC-600 dendrite and element mapping images of Co, Ni, O, C, and N, respectively (For interpretation of the references to colour in this figure legend, the reader is referred to the web version of this article).

existence of Co–O and Ni–O vibrations in CoNi/CoNiO<sub>2</sub>@NC-600 [50]. In addition, compared to Co<sub>0.75</sub>Ni<sub>0.25</sub> alloy dendrites, two peaks at 1355 and 1593 cm<sup>-1</sup> are observed in the Raman spectrum of CoNi/CoNiO<sub>2</sub>@NC-600 dendrites (Fig. 5d), which correspond to the D and G bands of carbon, respectively. The ratio of intensities of these two bands ( $I_D/I_G$ ) can evaluate degree of defect and disordered structures [51]. The  $I_D/I_G$  (1.06) reveals the high degree of disordered carbon in CoNi/CoNiO<sub>2</sub>@NC-600 dendrites. To better understand the functional group information, the Fourier transform infrared (FT-IR) spectrum of CoNi/CoNiO<sub>2</sub>@NC-600 dendrites was carried out. In Fig. S15, the absorption band at 605 cm<sup>-1</sup> is ascribed to the M–O (Co–O, Ni–O) [52], and the absorption band at 3396, 1637, and 1085 cm<sup>-1</sup> correspond to the characteristics of O–H, C=C, and C–OH stretching vibration [53], respectively, which further demonstrates the presence of CoNi oxides and hydrophilic group on the surface of N-doped carbon shell.

From the SEM image CoNi/CoNiO<sub>2</sub>@NC-600 (Fig. 6a), the flower-like dendrite structure is still well maintained. Furthermore, it is found that the rough carbon shell consisting of a great number of nanoparticles is attached on the surface of the dendrite structure (Fig. 6b). The nanoparticles have an average diameter of about 50 nm and are uniformly distributed on surface of the leaf. From the TEM image (Fig. 6c), the single leaf still maintains the intact morphology, and the difference of color of the small spots on the surface also demonstrates the uniform distribution of carbon nanoparticles. The HRTEM image (Fig. 6d) further displays the lattice fringes with the interplanar distances of 0.20 and 0.24 nm, which match well with the (111) plane of

fcc CoNi alloy phase and (111) plane of fcc CoNiO<sub>2</sub> phase. Furthermore, the corresponding SAED pattern in Fig. 6e reveals the polycrystalline nature of CoNi/CoNiO<sub>2</sub>@NC-600, and the diffraction rings are well indexed to (220) plane of CoNiO<sub>2</sub> and (111) plane of CoNi alloy. These results are consistent with the XRD analysis. Moreover, the EDX mapping analysis proves the coexistence and uniform distribution of Co, Ni, O, C, and N elements (Fig. 6f), the obvious distribution of C and N element confirms the successful doping of C and N in CoNi/CoNiO<sub>2</sub>@NC-600 dendrites.

The XPS survey spectrum of CoNi/CoNiO<sub>2</sub>@NC further shows the coexistence of Ni, Co, O, and C elements (Fig. 7a). According to the high-resolution Co 2p spectrum (Fig. 7b), the weak peaks at 778.5 eV (Co 2p<sub>3/2</sub>) and 793.0 eV (Co 2p<sub>1/2</sub>) are assigned to Co<sup>0</sup>, the peaks at 780.2 eV (Co 2p<sub>3/2</sub>) and 796.2 eV (Co 2p<sub>1/2</sub>) are ascribed to Co<sup>2+</sup>. The much higher intensity of Co<sup>2+</sup> peaks than metallic Co<sup>0</sup> peaks indicates the increased content of Co<sup>2+</sup> species after annealing [41]. For Ni 2p spectrum (Fig. 7c), the peaks at 852.5 eV (Ni 2p<sub>3/2</sub>) and 869.5 eV (Ni 2p<sub>1/2</sub>) can be attributed to Ni<sup>0</sup>, the peaks at 855.4 eV (Ni 2p<sub>3/2</sub>) and 872.6 eV (Ni 2p<sub>1/2</sub>) are characteristics of Ni<sup>2+</sup>. Similarly, the low intensity of metallic Ni<sup>0</sup> peaks suggests the deep coating of carbon and the increase of Ni<sup>2+</sup> species. In the O 1s spectrum (Fig. 7d), two strong peaks are clearly observed, the peak at 529.2 eV involves metal–oxygen bond and the peak at 531.3 eV involves surface hydroxyl groups [42]. The enhanced peak area of around 529.5 eV than that of Co<sub>0.75</sub>Ni<sub>0.25</sub> alloy (Fig. 3d) also confirms the increase of CoNi oxide components [23]. The peak at 532.9 eV is assigned to the adsorbed water. In

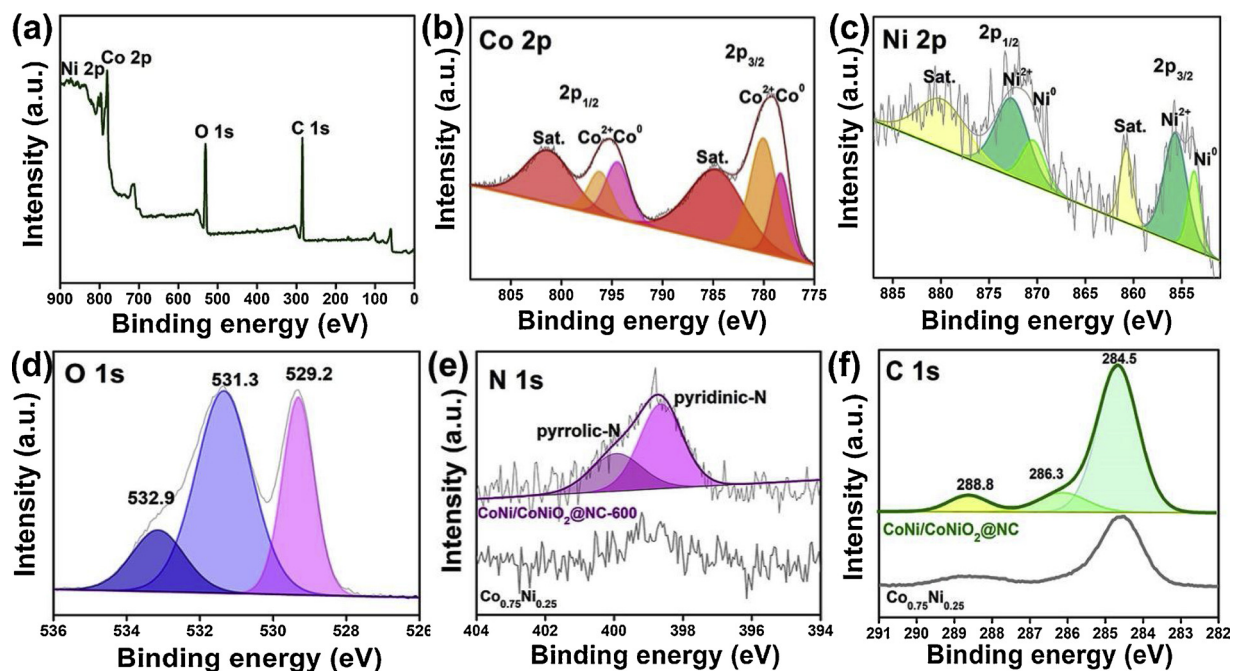


**Fig. 7.** (a) XPS survey of CoNi/CoNiO<sub>2</sub>@NC-600 dendrites. (b-d) High resolution XPS spectra of Co 2p, Ni 2p, and O 1s of CoNi/CoNiO<sub>2</sub>@NC-600 dendrites. (e) High resolution XPS spectra of N 1s of CoNi/CoNiO<sub>2</sub>@NC-600 dendrites and Co<sub>0.75</sub>Ni<sub>0.25</sub> alloy dendrites. (f) High resolution XPS spectra of C 1s of CoNi/CoNiO<sub>2</sub>@NC-600 dendrites and Co<sub>0.75</sub>Ni<sub>0.25</sub> alloy dendrites.

addition, the N 1s spectrum (Fig. 7e) is fitted with two peaks at 398.2 and 399.6 eV, which can be assigned to the pyridinic-N and pyrrolic-N, respectively, further revealing the N heteroatom doping [54]. The pyridinic-N is expected to show more effective electrochemical catalytic sites [55]. In the C 1s spectrum (Fig. 7f), two peaks at 284.5 and 288.8 eV can be indexed to C–C and C=O bond derived from the oxygen-contained groups in CoNi/CoNiO<sub>2</sub>@NC-600. The peak at 286.3 eV is corresponding to the C–N bond, further confirming the doping nitrogen in the carbon shell.

These dendrite-like CoNi-based products after annealing were dropped on CC to tests the OER performance in 1.0 M KOH. Fig. 8a, c show the *iR*-corrected OER polarization curves and Table S7 lists the overpotentials at the current densities of 10 and 100 mA cm<sup>-2</sup> of these catalysts. It is found that CoNi/CoNiO<sub>2</sub>@NC-600/CC shows the highest catalytic activity with the overpotentials at 10 and 100 mA cm<sup>-2</sup> of 1.411 V ( $\eta_{10} = 181$  mV) and 1.493 V ( $\eta_{100} = 263$  mV), respectively, and presents the lowest Tafel slope of 63 mV dec<sup>-1</sup>. To investigate the leading catalytic active centers of CoNi/CoNiO<sub>2</sub>@NC-600/CC composed of N-doped carbon, metal alloy, and metal oxide, N-doped carbon dropped on CC (NC/CC) and Co<sub>0.75</sub>Ni<sub>0.25</sub>/CC were first analyzed. It can be clearly seen that NC/CC slightly outperforms the bare CC in Fig. 8c, but Co<sub>0.75</sub>Ni<sub>0.25</sub>/CC still exhibits remarkably larger anode current density for OER than NC/CC, revealing the intrinsic activity sites of Co<sub>0.75</sub>Ni<sub>0.25</sub> alloy. Nevertheless, the alloy@carbon hybrid structures including CoNi@NC-300/CC, CoNi@NC-400/CC and CoNi@NC-500/CC display the obviously increased activity compared with Co<sub>0.75</sub>Ni<sub>0.25</sub>/CC without N-doped carbon (Fig. 8a and Table S7). The Tafel slopes also show a gradual decreasing trend (Fig. 8b, d), indicating that the introduction of N-doped carbon can accelerate the electron transfer rate and promote OER activity of Co<sub>0.75</sub>Ni<sub>0.25</sub> alloy. The CoNiO<sub>2</sub>@NC-700/CC without metal Co<sub>0.75</sub>Ni<sub>0.25</sub> exhibits inferior OER activity than CoNi/CoNiO<sub>2</sub>@NC-600/CC but superior to Co<sub>0.75</sub>Ni<sub>0.25</sub>/CC and NC/CC, which reveals that CoNiO<sub>2</sub> also plays a key role in the OER catalysis process. Therefore, it can be verified that CoNiO<sub>2</sub> and CoNi alloy jointly act as active centers of CoNi/CoNiO<sub>2</sub>@NC-600/CC to improve the catalytic activity of OER by synergistic effect, and N-doped carbon is favorable for the electron transfer of the whole electrode in the

electrochemical kinetics. In addition, bimetallic CoNi/CoNiO<sub>2</sub>@NC-600/CC also exhibits the higher activity than pure Co/CoO@NC-600/CC and Ni/NiO@NC-600/CC, demonstrating the mutual aid of Ni and Co in a way. Impressively, as an OER electrocatalyst, CoNi/CoNiO<sub>2</sub>@NC-600/CC is superior to commercial RuO<sub>2</sub>/CC and many recently reported earth-abundant OER catalysts (Table S8). The EIS measurements (at 250 mV) show that the CoNi/CoNiO<sub>2</sub>@NC-600/CC shows the smallest diameter of the semicircle, revealing the lowest charge-transfer resistance. On the CoNi/CoNiO<sub>2</sub>@NC-600/CC electrode, N-doped carbon shell, CoNiO<sub>2</sub> and CoNi alloy are combined into an interconnected conductive system: The electrons could transfer from the highly conductive carbon to CoNiO<sub>2</sub>, and then quickly transfer to the internal conductive CoNi alloy, which can form an effective electron transfer path to compensate for the lower conductivity of CoNiO<sub>2</sub> and reduce the charge-transfer resistance on the electrode surface.

The  $C_{dl}$  can estimate the effective ECSA, as shown in Fig. S17, CoNi/CoNiO<sub>2</sub>@NC-600/CC displays the largest  $C_{dl}$  value (50.21 m F cm<sup>-2</sup>) among CoNi@NC-300/CC (15.8 m F cm<sup>-2</sup>), CoNi@NC-400/CC (20.8 m F cm<sup>-2</sup>), CoNi@NC-500/CC (31.4 m F cm<sup>-2</sup>), and CoNiO<sub>2</sub>@NC-700/CC (21.8 m F cm<sup>-2</sup>), implying the larger ECSA and more effective active sites of CoNi/CoNiO<sub>2</sub>@NC-600/CC. The long-term cycling performance of CoNi/CoNiO<sub>2</sub>@NC-600/CC was evaluated (Fig. 8e), the polarization curve of Co<sub>0.75</sub>Ni<sub>0.25</sub>/CC shows a larger positive shift than that of CoNi/CoNiO<sub>2</sub>@NC-600/CC after 3000 and 6000 cycles, respectively. Fig. 8f shows the long-term stability of CoNi/CoNiO<sub>2</sub>@NC-600/CC tested at 1.42, 1.44, and 1.46 mV. As can be seen, CoNi/CoNiO<sub>2</sub>@NC-600/CC presents no obvious degradation by maintaining 95.6% ( $\eta = 1.42$  mV), 90.1% ( $\eta = 1.44$  mV), and 90.9% (1.46 mV) of its initial current density after 20 h of continuous operation, respectively, demonstrating again the remarkable durability. According to the atomic percentage of CoNi/CoNiO<sub>2</sub>@NC-600 dendrites after the OER stability test from the XPS (Table S9), it can be seen that the C content has a main loss after stability test, while the ratio of Co/Ni remains at 2.95 which just drops a little, suggesting that N-doped carbon shell can effectively relieve the corrosion of inner metal in rich oxygen bubble. The SEM image of CoNi/CoNiO<sub>2</sub>@NC-600 after stability test (Fig. S18) shows that the dendrite structure can firmly maintain,

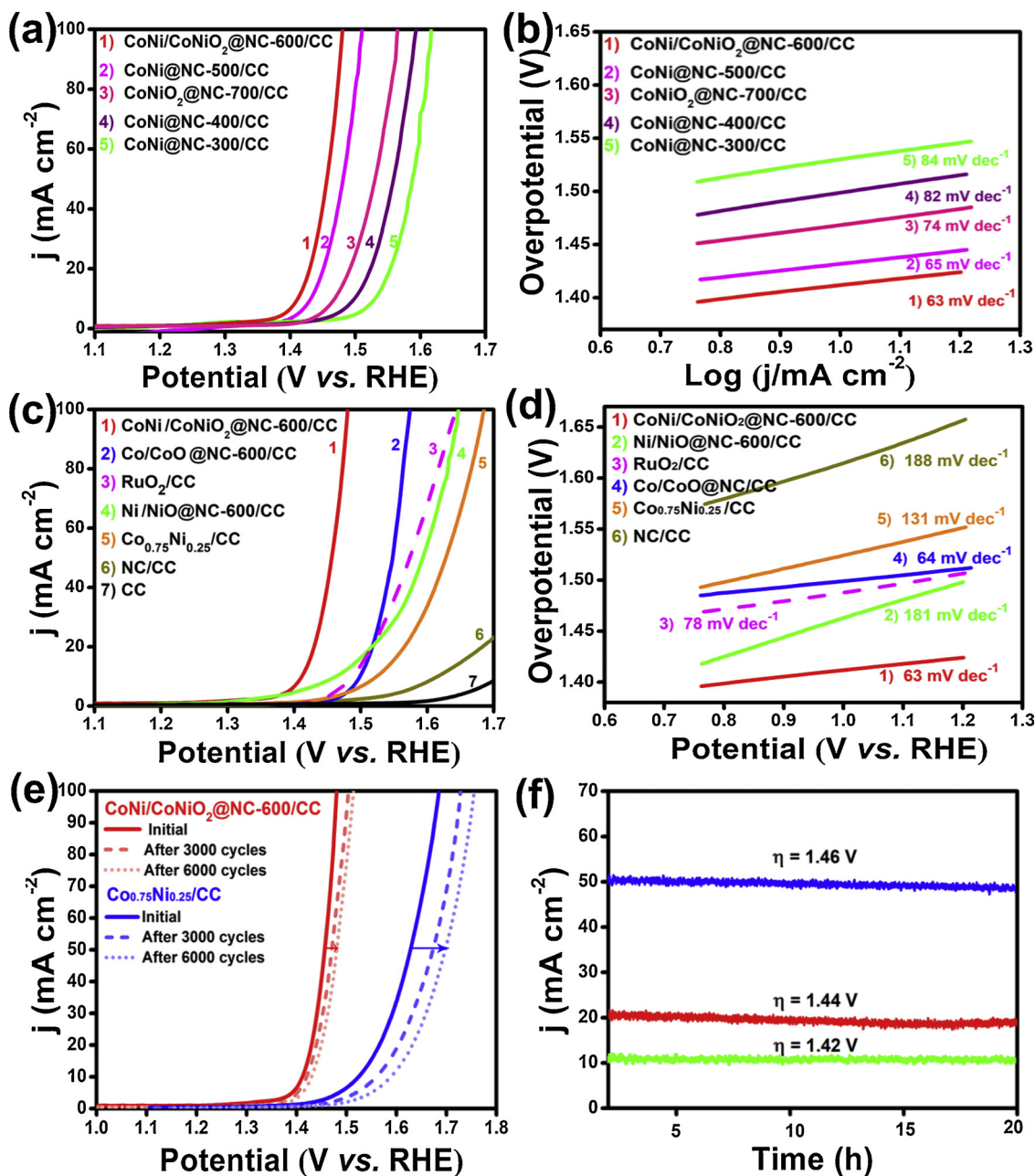


**Fig. 8.** Polarization curves (a) and Tafel plots (b) of CoNi@NC-300/CC, CoNi@NC-400/CC, CoNi@NC-500/CC, CoNi/CoNiO<sub>2</sub>@NC-600/CC, and CoNiO<sub>2</sub>@NC-700/CC in 1.0 M KOH. Polarization curves (c) and Tafel plots (d) of bare CC, NC/CC, Co<sub>0.75</sub>Ni<sub>0.25</sub>/CC, CoNi/CoNiO<sub>2</sub>@NC-600/CC, Co/CoO@NC/CC, Ni/NiO@NC-600/CC, and RuO<sub>2</sub>/CC in 1.0 M KOH. (e) Polarization curves for Co<sub>0.75</sub>Ni<sub>0.25</sub>/CC and CoNi/CoNiO<sub>2</sub>@NC-600/CC before and after 3000 and 6000 cycles of CV scanning. (f) Time-dependent current density curves of Co<sub>0.75</sub>Ni<sub>0.25</sub>/CC under the fixed overpotentials of 1.42, 1.44, and 1.46 V for 20 h, respectively.

and the signals of new phases are also undetectable in the XRD pattern (Fig. S19). However, the HRTEM image after the OER stability test shows a thin amorphous layer on the surface of CoNi/CoNiO<sub>2</sub>@NC-600 (Fig. S20), which might be the formed defect-rich NiCo-based oxy/hydroxides [56]. The peaks at 858.6 and 855.6 eV in the Ni 2p XPS spectrum after the OER stability test can be assigned to Ni<sup>3+</sup> and Ni<sup>2+</sup> (Fig. S21), indicating that NiOOH species in-situ formed on the catalyst surface.<sup>20</sup> In addition, the Raman spectrum (Fig. S22) shows that the peaks at 479 and 520 cm<sup>-1</sup> are assigned to the NiOOH, further confirming the emergence of Ni oxo/hydroxide species after stability test [57]. Thus, we may conclude that NiOOH formed on the catalyst surface also acts as an important active species for the OER.

Therefore, for CoNi/CoNiO<sub>2</sub>@NC-600/CC in our case, the enhanced OER catalytic activity can be ascribed to the following possible factors:

i). The novel hierarchical dendrite-like structure with rich active area would facilitate faster charge transfer and facile gas transport during the OER process. ii). The synergistic effects between CoNi alloy and CoNiO<sub>2</sub>, and the synergistic interaction between Ni/Co atoms would enhance the catalytic activity of OER. iii). The conductive and stable N-doped carbon shell coated the CoNi/CoNiO<sub>2</sub> dendrite offers a continuous highway for electron transfer throughout the integrated catalyst and optimizes the durability of the catalyst during the long-term operation. It is also necessary to test the HER performance of CoNi/CoNiO<sub>2</sub>@NC-600/CC in 1.0 M KOH (Fig. S23). CoNi/CoNiO<sub>2</sub>@NC-600/CC shows slightly inferior HER activity than Co<sub>0.75</sub>Ni<sub>0.25</sub>/CC, whereas presents better activity than CoNiO<sub>2</sub>/NC-700/CC, inferring that the thicker CoNiO<sub>2</sub> layer with lower conductivity would barrier the charge transfer to internal metal active center.

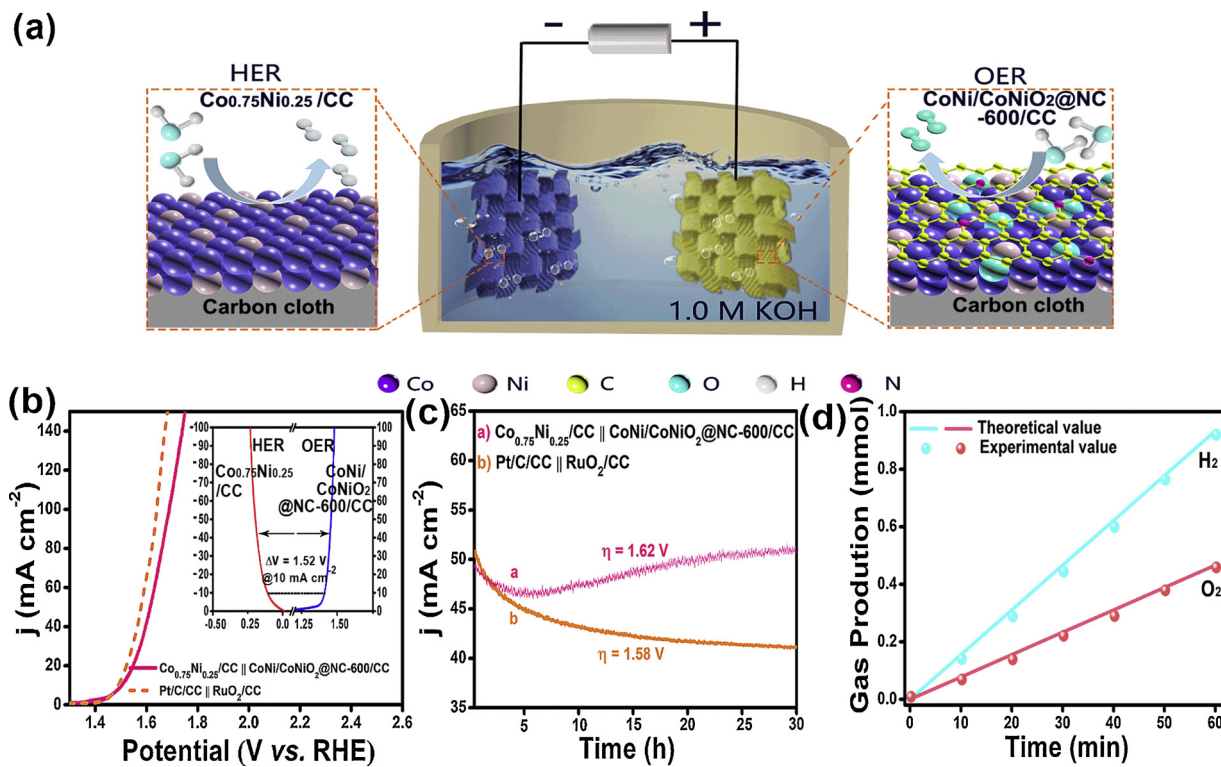


**Fig. 9.** (a) Schematic set-up of the alkaline water splitting device. (b) *iR*-corrected polarization curves of  $\text{Co}_{0.75}\text{Ni}_{0.25}/\text{CC} \parallel \text{CoNi/CoNiO}_2/\text{NC-600}/\text{CC}$  and  $\text{Pt/C/CC} \parallel \text{RuO}_2/\text{CC}$ . The inset of (b) is the *iR*-corrected polarization curves of  $\text{Co}_{0.75}\text{Ni}_{0.25}/\text{CC}$  for HER and  $\text{CoNi/CoNiO}_2/\text{NC-600}/\text{CC}$  for OER. (c) Time-dependent current density curves of  $\text{Co}_{0.75}\text{Ni}_{0.25}/\text{CC} \parallel \text{CoNi/CoNiO}_2/\text{NC-600}/\text{CC}$  (at 1.62 V) and  $\text{Pt/C/CC} \parallel \text{RuO}_2/\text{CC}$  (at 1.58 V). (d) Experimental and theoretical amounts of  $\text{H}_2$  catalyzed by  $\text{Co}_{0.75}\text{Ni}_{0.25}/\text{CC}$  and  $\text{O}_2$  catalyzed by  $\text{CoNi/CoNiO}_2/\text{NC-600}/\text{CC}$  in 1.0 M KOH, respectively, at a fixed current density of  $50 \text{ mA cm}^{-2}$ .

### 3.3. Overall water splitting

Based on the outstanding HER activity of  $\text{Co}_{0.75}\text{Ni}_{0.25}/\text{CC}$  and the excellent OER activity of  $\text{CoNi/CoNiO}_2/\text{NC-600}/\text{CC}$  in the same alkaline electrolyte, we designed a water splitting device with  $\text{Co}_{0.75}\text{Ni}_{0.25}/\text{CC}$  as the cathode and  $\text{CoNi/CoNiO}_2/\text{NC-600}/\text{CC}$  as the anode (denoted as  $\text{Co}_{0.75}\text{Ni}_{0.25}/\text{CC} \parallel \text{CoNi/CoNiO}_2/\text{NC-600}/\text{CC}$ ) in 1.0 M KOH. The electrolyzation schematic diagram of the  $\text{Co}_{0.75}\text{Ni}_{0.25}/\text{CC} \parallel \text{CoNi/CoNiO}_2/\text{NC-600}/\text{CC}$  system is displayed in Fig. 9a. According to the *iR*-corrected polarization curves (Fig. 9b), the  $\text{Co}_{0.75}\text{Ni}_{0.25}/\text{CC} \parallel \text{CoNi/CoNiO}_2/\text{NC-600}/\text{CC}$  system displays excellent catalytic performance with a cell voltage of 1.51 V to deliver a current density of  $10 \text{ mA cm}^{-2}$ , which is closed to the voltage difference ( $\Delta V = 1.52 \text{ V}$ ) between HER and OER at the same current density of  $10 \text{ mA cm}^{-2}$  (inset of Fig. 9b). Moreover, the cell voltage is only 30 mV larger than that of  $\text{Pt/C/CC} \parallel \text{RuO}_2/\text{CC}$  ( $1.49 \text{ V}$  at  $10 \text{ mA cm}^{-2}$ ) and comparable to many previously reported water splitting electrocatalysts (see Table S10). Impressively, the  $\text{Co}_{0.75}\text{Ni}_{0.25}/\text{CC} \parallel \text{CoNi/CoNiO}_2/\text{NC-600}/\text{CC}$  exhibits better stability than the  $\text{Pt/C/CC} \parallel \text{RuO}_2/\text{CC}$  after 30 h of electrolysis (Fig. 9c), and the current density driven at 1.63 V has a slight increase of  $2 \text{ mA cm}^{-2}$  than initial value, whereas the current density driven by  $\text{Pt/C/CC} \parallel \text{RuO}_2/\text{CC}$  at 1.58 V has a distinct decrease of  $11 \text{ mA cm}^{-2}$ . Additionally, the Faraday efficiency was measured to analyze the utilization efficiency of electrons participation. From Fig. 9d, the amounts of generated  $\text{H}_2$  and  $\text{O}_2$  quantified by gas chromatography are in good agreement with that of theoretically calculated value at a constant current density of  $50 \text{ mA cm}^{-2}$ , and the average evolution rates of  $\text{H}_2$  and  $\text{O}_2$  obtained from the linear slope of the generated gas amount versus electrolysis time are approximately  $1.53 \times 10^{-2}$  and  $7.57 \times 10^{-3} \text{ mmol min}^{-1}$ , respectively, revealing a nearly 2:1 ratio of  $\text{H}_2$  to  $\text{O}_2$ . The Faraday efficiency for HER and OER were calculated to be 98.5% and 97.4%, respectively, demonstrating that the current was attributed to water splitting. These results indicate that our Co-Ni based dendrite system is

an attractive electrocatalyst candidate toward water splitting based on the high electrocatalytic activity and excellent stability.

### 4. Conclusion

In summary, unique hierarchical  $\text{Co}_{0.75}\text{Ni}_{0.25}$  alloy dendrites have been successfully synthesized through a facile hydrothermal method and can serve as a highly efficient HER electrocatalyst. By adjusting the molar ratio of metal (Co and Ni) sources used during synthesis, the morphology, size, and catalytic performance of CoNi alloy dendrites were synergistically modulated. The dendrite-like  $\text{Co}_{0.75}\text{Ni}_{0.25}/\text{CC}$  electrode shows high activity and stability as the HER catalyst than the nanoplate-like  $\text{Co}_{0.75}\text{Ni}_{0.25}/\text{CC}$  electrode due to its more effective active sites provided by the dendrite structure. Based on the unique hierarchical structure of  $\text{Co}_{0.75}\text{Ni}_{0.25}$  alloy dendrites, the OER performance has an obvious improvement due to the introduction of *in-situ* formed  $\text{CoNiO}_2$  and N-doped carbon shell. The synergistic effects from CoNi alloy,  $\text{CoNiO}_2$ , and the conductive N-doped carbon shell effectively enhance catalytic OER activity, while the complementary design and synthesis of these Co-Ni based dendrite materials allow for efficiency optimization and cost reduction. As expected, when assembling  $\text{Co}_{0.75}\text{Ni}_{0.25}/\text{CC}$  and  $\text{CoNi/CoNiO}_2/\text{NC-600}/\text{CC}$  together to construct overall water splitting device,  $\text{Co}_{0.75}\text{Ni}_{0.25}/\text{CC} \parallel \text{CoNi/CoNiO}_2/\text{NC-600}/\text{CC}$  needs a cell voltage of only about 1.51 V to achieve  $10 \text{ mA cm}^{-2}$  and possess excellent stability in 1.0 M KOH. This work may open up a new strategy to develop efficient non-noble metal catalysts in designing and exploring more novel structures and compositions with synergistic catalytic effects.

### Acknowledgments

Authors acknowledge financial support for this work from the Natural Science Foundation of Chongqing (No. CSTC-2015jcyjB50001)

and the National Natural Science Foundation of China (No. 21675131).

## Appendix A. Supplementary data

Supplementary material related to this article can be found, in the online version, at doi:<https://doi.org/10.1016/j.apcatb.2019.05.035>.

## References

- [1] X. Zou, Y. Zhang, Noble metal-free hydrogen evolution catalysts for water splitting, *Chem. Soc. Rev.* 44 (2015) 5148–5180.
- [2] Z.W. Seh, J. Kibsgaard, C.F. Dickens, I. Chorkendorff, J.K. Nørskov, T.F. Jaramillo, Combining theory and experiment in electrocatalysis: insights into materials design, *Science* 355 (2017) eaad4998.
- [3] R. Subbaraman, D. Tripkovic, K.-C. Chang, D. Strmcniak, A.P. Paulikas, P. Hirunsit, M. Chan, J. Greeley, V. Stamenkovic, N.M. Markovic, Trends in activity for the water electrolyser reactions on 3D M (Ni, Co, Fe, Mn) hydr(oxy)oxide catalysts, *Nat. Mater.* 11 (2012) 550–557.
- [4] Y. Jiao, Y. Zheng, M. Jaroniec, S.Z. Qiao, Design of electrocatalysts for oxygen and hydrogen-involving energy conversion reactions, *Chem. Soc. Rev.* 44 (2015) 2060–2086.
- [5] J. Feng, L. Ding, S. Ye, X. He, H. Xu, Y. Tong, G. Li,  $\text{Co(OH)}_2@\text{PANI}$  hybrid nanosheets with 3d networks as high-performance electrocatalysts for hydrogen evolution reaction, *Adv. Mater.* 27 (2015) 7051–7057.
- [6] C.G. Morales-Guio, L. Liardet, X. Hu, Oxidatively electrodeposited thin-film transition metal (oxy)hydroxides as oxygen evolution catalysts, *J. Am. Chem. Soc.* 138 (2016) 8946–8957.
- [7] E. Jung, H.-Y. Park, A. Cho, J.H. Jang, H.S. Park, T. Yu, Aqueous-phase synthesis of metal hydroxide nanoplates and platinum/nickel hydroxide hybrid nanostructures and their enhanced electrocatalytic properties, *Appl. Catal. B: Environ.* 225 (2018) 238–242.
- [8] A. Grimaud, K.J. May, C.E. Carlton, Y.-L. Lee, M. Risch, W.T. Hong, J.G. Zhou, Y. Shao-Horn, An advanced Ni-Fe layered double hydroxide electrocatalyst for water oxidation, *Nat. Commun.* 4 (2439) (2013).
- [9] G. Gardner, J. Al-Sharab, N. Danilovic, Y.B. Go, K. Ayers, M. Greenblatt, G.C. Dismukes, Structural basis for differing electrocatalytic water oxidation by the cubic, layered and spinel forms of lithium cobalt oxides, *Energy Environ. Sci.* 9 (2016) 184–192.
- [10] Q. Zhang, C. Ye, X.L. Li, Y.H. Deng, B.X. Tao, W. Xiao, L.J. Li, N.B. Li, H.Q. Luo, Self-interconnected porous networks of NiCo disulfide as efficient bifunctional electrocatalysts for overall water splitting, *ACS Appl. Mater. Interfaces* 10 (2018) 27723–27733.
- [11] Y. Yang, W. Zhang, Y. Xiao, Z. Shi, X. Cao, Y. Tang, Q. Gao,  $\text{CoNiSe}_2$  heteronanoarrays decorated with layered-double-hydroxides for efficient hydrogen evolution, *Appl. Catal. B* 242 (2019) 132–139.
- [12] R. Michalsky, Y.J. Zhang, A.A. Peterson, Trends in the hydrogen evolution activity of metal carbide catalysts, *ACS Catal.* 4 (2014) 1274–1278.
- [13] S. Jing, L. Zhang, L. Luo, J. Lu, S. Yin, P.K. Shen, P. Tsiaikaras, N-doped porous molybdenum carbide nanobelts as efficient catalysts for hydrogen evolution reaction, *Appl. Catal. B: Environ.* 224 (2018) 533–540.
- [14] X. Li, W. Liu, M. Zhang, Y. Zhong, Z. Weng, Y. Mi, Y. Zhou, M. Li, J.J. Cha, Z. Tang, H. Jiang, X. Li, H. Wang, Strong metal-phosphide interactions in core-shell geometry for enhanced electrocatalysis, *Nano Lett.* 17 (2017) 2057–2063.
- [15] C. Ye, M.Q. Wang, G. Chen, Y.H. Deng, L.J. Li, H.Q. Luo, N.B. Li, One-step CVD synthesis of carbon framework wrapped  $\text{Co}_2\text{P}$  as a flexible electrocatalyst for efficient hydrogen evolution, *J. Mater. Chem. A Mater. Energy Sustain.* 5 (2017) 7791–7795.
- [16] Q. Sun, Y. Dong, Z. Wang, S. Yin, C. Zhao, Synergistic nanotubular copper-doped nickel catalysts for hydrogen evolution reactions, *Small* 14 (2018) 1704137.
- [17] J.X. Feng, J.Q. Wu, Y.X. Tong, G.R. Li, Efficient hydrogen evolution on cu nanodots-decorated  $\text{Ni}_3\text{S}_2$  nanotubes by optimizing atomic hydrogen adsorption and desorption, *J. Am. Chem. Soc.* 140 (2018) 610–617.
- [18] J.R. McKone, B.F. Sadler, C.A. Werlang, N.S. Lewis, H.B. Gray, Ni-Mo nanopowders for efficient electrochemical hydrogen evolution, *ACS Catal.* 3 (2013) 166–169.
- [19] V.M. Nikolic, S.L. Maslovaraa, G.S. Tasic, T.P. Brdaric, P.Z. Lausevic, B.B. Radaka, M.P.M. Kaninski, Kinetics of hydrogen evolution reaction in alkaline electrolysis on a Ni cathode in the presence of Ni-Co-Mo based ionic activators, *Appl. Catal. B Environ.* 179 (2015) 88–94.
- [20] X. Xu, H. Liang, F. Ming, Z. Qi, Y. Xie, Z. Wang, Prussian blue analogues derived penroseite ( $\text{Ni},\text{Co}\text{Se}_2$ ) nanocages anchored on 3D graphene aerogel for efficient water splitting, *ACS Catal.* 7 (2017) 6394–6399.
- [21] S. Li, Y. Wang, S. Peng, L. Zhang, A.M. Al-Enizi, H. Zhang, X. Sun, G. Zheng, Co-Ni-based nanotubes/nanosheets as efficient water splitting electrocatalysts, *Adv. Energy Mater.* 6 (2016) 1501661.
- [22] K. Fominykh, G.C. Tok, P. Zeller, H. Hajiyani, T. Miller, M. Döblinger, R. Pentcheva, T. Bein, D.F. Rohlfing, Salt Ni/Co oxides with unusual nanoscale-stabilized composition as water splitting electrocatalysts, *Adv. Funct. Mater.* 27 (2017) 1605121.
- [23] S.Hu. Bae, J.E. Kim, H. Randriamahazaka, Y.M. Song, J.Y. Park, I.K. Oh, Seamlessly conductive 3D nanoarchitecture of core-shell Ni-Co nanowire network for highly efficient oxygen evolution, *Adv. Energy Mater.* 7 (2016) 1601492.
- [24] X. Cui, P. Xiao, J. Wang, M. Zhou, W. Guo, Y. Yang, Y. He, Z. Wang, Y. Yang, Y. Zhang, Z. Lin, Highly branched metal alloy networks with superior activities for the methanol oxidation reaction, *Angew. Chem. Int. Ed.* 129 (2017) 1–7.
- [25] L. Lin, Z. Sun, M. Yuan, J. He, R. Long, H. Li, C. Nan, G. Sun, S. Ma, Significant enhancement of the performance of hydrogen evolution reaction through shape-controlled synthesis of hierarchical dendrite-like platinum, *J. Mater. Chem. A Mater. Energy Sustain.* 6 (2018) 8068–8077.
- [26] S. Mao, Z. Wen, T. Huang, Y. Hou, J. Chen, High-performance Bi-functional electrocatalysts of 3D crumpled graphene-cobalt oxide nanohybrids for oxygen reduction and evolution reactions, *Energy Environ. Sci.* 7 (2014) 609–616.
- [27] T. Zhang, M.-Y. Wu, D.-Y. Yan, J. Maoa, H. Liu, W.-B. Hu, X.-W. Du, T. Ling, S.-Z. Qiao, Engineering oxygen vacancy on NiO nanorod arrays for alkaline hydrogen evolution, *Nano Energy* 43 (2018) 103–109.
- [28] Y.P. Zhu, Y.M. Tian, M. Jaroniec, S.Z. Qiao, Self-templating synthesis of hollow  $\text{Co}_3\text{O}_4$  microtube arrays for highly efficient water electrolysis, *Angew. Chem. Int. Ed.* 55 (2016) 1–6.
- [29] J. Huang, J. Han, R. Wang, Y. Zhang, X. Wang, X. Zhang, Z. Zhang, Y. Zhang, B. Song, S. Jin, Improving electrocatalysts for oxygen evolution using  $\text{Ni}_{x}\text{Fe}_{3-x}\text{O}_4/\text{Ni}$  hybrid nanostructures formed by solvothermal synthesis, *ACS Energy Lett.* 3 (2018) 1698–1707.
- [30] X.F. Lu, L.F. Gu, J.W. Wang, J.X. Wu, P.Q. Liao, G.R. Li, Bimetal-organic framework derived  $\text{CoFe}_2\text{O}_4/\text{C}$  porous hybrid nanorod arrays as high-performance electrocatalysts for oxygen evolution reaction, *Adv. Mater.* 29 (2017) 1604437.
- [31] L. Zhuang, L. Ge, Y. Yang, M. Li, Y. Jia, X. Yao, Z. Zhu, Ultrathin iron-cobalt oxide nanosheets with abundant oxygen vacancies for the oxygen evolution reaction, *Adv. Mater.* 29 (2017) 1606793.
- [32] X. Yan, L. Tian, M. He, X. Chen, Three-dimensional crystalline/amorphous  $\text{Co}/\text{Co}_3\text{O}_4$  core/shell nanosheets as efficient electrocatalysts for the hydrogen evolution reaction, *Nano Lett.* 15 (2015) 6015.
- [33] X. Yan, L. Tian, X. Chen, Crystalline/amorphous  $\text{Ni}/\text{NiO}$  core/shell nanosheets as highly active electrocatalysts for hydrogen evolution reaction, *J. Power Sources* 300 (2015) 336–343.
- [34] C. Tang, N.Y. Cheng, Z.H. Pu, W. Xing, X.P. Sun, NiSe nanowire film supported on nickel foam: an efficient and stable 3D bifunctional electrode for full water splitting, *Angew. Chem.* 127 (2015) 9483–9487.
- [35] M. Gong, Y. Li, H. Wang, Y. Liang, J.Z. Wu, J. Zhou, J. Wang, T. Regier, F. Wei, H. Dai, An advanced Ni-Fe layered double hydroxide electrocatalyst for water oxidation, *J. Am. Chem. Soc.* 135 (2013) 8452–8455.
- [36] R. Yang, Y. Zhou, Y. Xing, D. Li, D. Jiang, M. Chen, W. Shi, S. Yuan, Synergistic coupling of CoFe-LDH arrays with NiFe-LDH nanosheet for highly efficient overall water splitting in alkaline media, *Appl. Catal. B* 253 (2019) 131–139.
- [37] X.-M. Zhou, X.-W. Wei, Single crystalline  $\text{FeNi}_3$  dendrites: large scale synthesis, formation mechanism, and magnetic properties, *Cryst. Growth Des.* 9 (2009) 7–12.
- [38] L.-P. Zhu, H.-M. Xiao, W.-D. Zhang, Y. Yang, S.-Y. Fu, Synthesis and characterization of novel three-dimensional metallic Co dendritic superstructures by a simple hydrothermal reduction route, *Cryst. Growth Des.* 8 (2008) 1113–1118.
- [39] T.C.S.C. Gomes, J.D.L.T. Medina, M. Lemaitre, L. Piriaux, Magnetic and magnetoresistive properties of 3d interconnected NiCo nanowire networks, *Nanoscale Res. Lett.* 11 (2016) 466.
- [40] M. Cheng, M. Wen, S. Zhou, Q. Wu, B. Sun, Solvothermal synthesis of NiCo alloy icosahedral nanocrystals, *Inorg. Chem.* 51 (2012) 1495–1500.
- [41] V.F. Puntes, D. Zanchet, C.K. Erdonmez, A.P. Alivisatos, Synthesis of hcp-Co nanodisks, *J. Am. Chem. Soc.* 124 (2002) 12874–12880.
- [42] H. Jin, J. Wang, D. Su, Z. Wei, Z. Pang, Y. Wang, In-situ cobalt-cobalt oxide/n-doped carbon hybrids as superior bifunctional electrocatalysts for hydrogen and oxygen evolution, *J. Am. Chem. Soc.* 137 (2015) 2688–2694.
- [43] Y. Kim, D.H.K. Jackson, D. Lee, M. Choi, T.-W. Kim, S.-Y. Jeong, H.-J. Chae, H.-W. Kim, N.H. Park, T. Chang, F. Kuech, H.J. Kim, In situ electrochemical activation of atomic layer deposition coated  $\text{MoS}_2$  basal planes for efficient hydrogen evolution reaction, *Adv. Funct. Mater.* 27 (2017) 1701825.
- [44] W. Sheng, M. Myint, J.G. Chen, Y. Yan, Correlating the hydrogen evolution reaction activity in alkaline electrolytes with the hydrogen binding energy on monometallic surfaces, *Energy Environ. Sci.* 6 (2013) 1509–1512.
- [45] S.C. Petitto, E.M. Marsh, G.A. Carson, M.A. Langell, Cobalt oxide surface chemistry: the interaction of  $\text{CoO}$  (100),  $\text{Co}_3\text{O}_4$  (110) and  $\text{Co}_3\text{O}_4$  (111) with oxygen and water, *J. Mol. Catal. A Chem.* 281 (2008) 49–58.
- [46] Y. Yan, B.Y. Xia, Z. Xu, X. Wang, Recent development of molybdenum sulfides as advanced electrocatalysts for hydrogen evolution reaction, *ACS Catal.* 4 (2014) 1693–1705.
- [47] D.Y. Chung, S.W. Jun, G. Yoon, H. Kim, J.M. Yoo, K.-S. Lee, T. Kim, H. Shin, A.K. Sinha, S.G. Kwon, K. Kang, T. Hyeon, Y.-E. Sung, Large-scale synthesis of carbon-shell-coated FeP nanoparticles for robust hydrogen evolution reaction electrocatalyst, *J. Am. Chem. Soc.* 139 (2017) 6669–6674.
- [48] H. Sato, O. Kitakami, T. Sakurai, Y. Shimada, Y. Otani, K. Fukamichi, Structure and magnetism of hcp-Co fine particles, *J. Appl. Phys.* 81 (1997) 1858–1862.
- [49] F. Wu, S. Zhang, B. Xi, Z. Feng, D. Sun, X. Ma, J. Zhang, J. Feng, S. Xiong, Unusual formation of  $\text{CoO}@\text{C}$  “dandelions” derived from 2D Kagome MOLs for efficient lithium storage, *Adv. Energy Mater.* 8 (2018) 1703242.
- [50] Y. Liu, G. Han, X. Zhang, C. Xing, C. Du, H. Cao, B. Li,  $\text{Co}-\text{Co}_3\text{O}_4@\text{carbon}$  core–shells derived from metal-organic framework nanocrystals as efficient hydrogen evolution catalysts, *Nano Res.* 10 (2017) 3035–3048.
- [51] C. Lu, D. Tranca, J. Zhang, F.R. Hernandez, Y. Su, X. Zhuang, F. Zhang, G. Seifert, X. Feng, Molybdenum carbide-embedded nitrogen-doped porous carbon nanosheets as electrocatalysts for water splitting in alkaline media, *ACS Nano* 11 (2017) 3933–3942.
- [52] K. Jayaramulu, J. Masa, O. Tomanec, D. Peeters, V. Ranc, A. Schneemann, R. Zboril, W. Schuhmann, R.A. Fischer, *Adv. Funct. Mater.* 27 (2017) 1700451.
- [53] Y.-Y. Ma, C.-X. Wu, X.-J. Feng, H.-Q. Tan, L.K. Yan, Y. Liu, Z.-H. Kang, E.-B. Wang, Y.-G. Li, Nanoporous nitrogen-doped graphene oxide/nickel sulfide composite

- sheets derived from a metal-organic framework as an efficient electrocatalyst for hydrogen and oxygen evolution, *Energy Environ. Sci.* 10 (2017) 788–798.
- [54] M.-S. Balogun, W. Qiu, H. Yang, W. Fan, Y. Huang, P. Fang, G. Li, H. Ji, Y. Tong, A monolithic metal-free electrocatalyst for oxygen evolution reaction and overall water splitting, *Energy Environ. Sci.* 9 (2016) 3411–3416.
- [55] X. Li, J. Wei, Q. Li, S. Zheng, Y. Xu, P. Du, C. Chen, J. Zhao, H. Xue, Q. Xu, H. Pang, Nitrogen-doped cobalt oxide nanostructures derived from cobalt-alanine complexes for high-performance oxygen evolution reactions, *Adv. Funct. Mater.* 28 (2018) 1800886.
- [56] Z. Chen, L. Cai, X. Yang, C. Kronawitter, L. Guo, S. Shen, B.E. Koel, Reversible structural evolution of  $\text{NiCo}_{0.8}\text{H}_y$  during the oxygen evolution reaction and identification of the catalytically active phase, *ACS Catal.* 8 (2018) 1238–1247.
- [57] Y. Li, H. Zhang, M. Jiang, Q. Zhang, P. He, X. Sun, 3D self-supported Fe-doped  $\text{Ni}_2\text{P}$  nanosheet arrays as bifunctional catalysts for overall water splitting, *Adv. Funct. Mater.* 27 (2017) 1702513.